**Universidade de Aveiro**
**2019**
Departamento de Engenharia de Materiais e Cerâmica

**BERNARDO FILIPE SERÔDIO COSTA**

# Ni-Sr(V,Ti,Ni)$O_3$ ELECTRODES FOR REVERSIBLE SOLID ELECTROLYTE CELLS

# ELÉTRODOS Ni-Sr(V,Ti,Ni)$O_3$ PARA PILHAS DE COMBUSTÍVEL REVERSÍVEIS

**Universidade de Aveiro**
**2019**

Departamento de Engenharia de Materiais e Cerâmica

**BERNARDO FILIPE SERÔDIO COSTA**

# Ni-Sr(V,Ti,Ni)$O_3$ ELECTRODES FOR REVERSIBLE SOLID ELECTROLYTE CELLS

# ELÉTRODOS Ni-Sr(V,Ti,Ni)$O_3$ PARA PILHAS DE COMBUSTÍVEL REVERSÍVEIS

Dissertação apresentada à Universidade de Aveiro para cumprimento dos requisitos necessários à obtenção do grau de mestre em Mestrado Integrado em Engenharia dos Materiais, realizada sob a orientação científica do Doutor Aleksey Yaremchenko, Investigador Doutorado do Departamento de Engenharia de Materiais e Cerâmica da Universidade de Aveiro, e da Doutora Blanca I. Arias-Serrano, Estagiária de Pós-Doutoramento do Departamento de Engenharia de Materiais e Cerâmica da Universidade de Aveiro.

O trabalho desta tese foi realizado no âmbito do projeto CARBOSTEAM - POCI-01-0145-FEDER-032295, suportado pelos orçamentos do Programa Operacional POCI, na sua componente FEDER, e da Fundação para a Ciência e a Tecnologia, na sua componente de Orçamento de Estado.

♫ All My Friends

**o júri**

presidente

Prof. Doutor Fernando Manuel Bico Marques
professor catedrático da Universidade de Aveiro

Doutor Duncan Paul Fagg
equiparado a investigador principal da Universidade de Aveiro

Doutor Aleksey Yaremchenko
investigador doutorado (Nível 1) da Universidade de Aveiro

**agradecimentos**

First and foremost, I would like to thank my supervisors, Dr. Yaremchenko and Dr. Arias-Serrano, for their full guidance, support and patience on my experimental work. None of this would be possible without your cooperation, and I enjoyed working with you very much. I would like to mention and thank Prof. Frade as well for his very initial contribute on this work, as well as Dr. Kavaleuski.

I want to thank all my colleagues from DEMaC, specially those who were involved even in the slightest with this work and with whom I shared a workplace in labs 9.2.3, 9.2.8 and 9.2.9 this last year. Your warm presence and companionship kept me going. Muito obrigado por tudo, thank you all for everything, спасибо вам за все, muchas gracias por todo.

Finalmente, um obrigado a todos os meus amigos e família pelo seu apoio.

À Sílvia, o meu maior obrigado pelo maior apoio de todos.

**palavras-chave**

Célula de combustível, célula de electrólise, célula de combustível reversível, eléctrodo de combustível, titanato de estrôncio, vanadato de estrôncio, exsolução, condutividade eléctrica, expansão térmica, resistência de polarização.

**resumo**

O principal objetivo deste trabalho foi avaliar a possibilidade de melhoria da atividade eletrocatalítica de elétrodos de combustível $Sr(Ti,V)O_{3-\delta}$ utilizados em eletrólitos de alta temperatura, introduzindo Ni na subrede B da estrutura do tipo perovskite, com nanoestruturação in-situ em condições de operação por via de exsolução. Este trabalho teve como motivação as desvantagens associadas ao uso típico de ânodos cermet Ni-YSZ, como degradação da microestrutura a longo termo e intolerância a mudanças redox, contaminação de enxofre e deposição de carbono. Foi considerado o uso de titanato-vanadato de estrôncio como componentes cerâmicos adequados dentro das condições de operação de elétrodos de combustível e com vista a tolerar a deposição de carbono e enxofre, enquanto se perspectivava que Ni nano-dispersado pudesse aumentar a atividade eletrocatalítica, evitando as desvantagens associadas ao cermet Ni-YSZ.

Tratamentos mecanoquímicos de alta energia, em combinação com tratamentos térmicos sob atmosferas redutoras foram aplicados na preparação dos materiais selecionados de composição nominal $Sr_{1-x}Ti_{1-y-z}V_yNi_zO_3$ ($x$ = 0-0.04, $y$ = 0.2-0.4, $z$ = 0.02-0.12). Análise detalhada à formação de fases no sistema revelou que é necessário um tratamento térmico de relativamente alta temperatura (1200 °C) de modo a eliminar a fase intermédia $Sr_3(VO_4)_2$, indesejada no curso da síntese de perovskites do tipo $Sr(Ti,V)O_3$, que resulta na segregação do Ni na forma de partículas metálicas abaixo do mícron, deficientemente dispersas.

Os cerâmicos $Sr_{1-x}(Ti,V)O_{3-\delta}$-Ni preparados exibiram um coeficiente de expansão térmica moderado, comparativamente ao do eletrólito utilizado YSZ. A condutividade elétrica provou-se aumentar em função da quantidade de vanádio na perovskite, enquanto que deficiência nominal no elemento A provocaria o efeito oposto. Estudos na espectroscopia de impedância eletroquímica revelaram fraca atividade dos elétrodos porosos $Sr_{1-x}(Ti,V)O_{3-\delta}$-Ni em oxidação de hidrogénio. Isto foi atribuído a uma atividade eletrocatalítica intrinsecamente insuficiente, fraca condução iónica destas fases e segregação das partículas de Ni no decorrer da síntese. Ficou demonstrado que a performance eletroquímica destes elétrodos pode ser substancialmente melhorada com a infiltração de soluções contendo Céria dopada com Gadolínia, usada como condutor iónico de oxigénio, assim como soluções da mesma contendo Ni bem disperso de modo a atuar como catalizador.

**keywords**

Solid oxide fuel cell, solid oxide electrolysis cell, reversible solid oxide cell, fuel electrode, strontium titanate, strontium vanadate, exsolution, electrical conductivity, thermal expansion, polarization resistance

**abstract**

The main objective of this work was to assess the possibility of the enhancement of the electrocatalytic activity of $Sr(Ti,V)O_{3-\delta}$ fuel electrode components for high-temperature solid electrolyte cells by introducing Ni into the B-sublattice of the perovskite structure with in-situ nanostructuring under operation conditions by exsolution. The work was motivated by the drawbacks of commonly used cermet Ni-YSZ cermet anodes such as long-term microstructural degradation and intolerance to redox changes, sulfur poisoning and carbon deposition. Strontium titanate-vanadates were considered as suitable ceramic components stable under fuel electrode operation conditions and with prospects for sulfur and carbon deposition tolerance, while nano-dispersed Ni was expected to enhance the electrocatalytic activity while avoiding the disadvantages of Ni-YSZ cermets.

High-energy mechanochemical route in combination with thermal treatments under controlled reducing atmosphere were employed for the preparation of selected materials with a nominal composition $Sr_{1-x}Ti_{1-y-z}V_yNi_zO_3$ ($x$ = 0-0.04, $y$ = 0.2-0.4, $z$ = 0.02-0.12). Detailed analysis of the phase formation in this system revealed that comparatively high thermal treatment temperature (1200°C), required to eliminate the undesired insulating $Sr_3(VO_4)_2$ intermediate phase in the course of synthesis of $Sr(Ti,V)O_3$ perovskites, results in a segregation of Ni in the form of poorly dispersed submicron metallic particles.

Prepared $Sr_{1-x}(Ti,V)O_{3-\delta}$-Ni ceramic materials exhibited a moderate thermal expansion coefficients compatible with that of YSZ solid electrolyte. The electrical conductivity was found to increase with increasing vanadium content in the perovskite phase, while the nominal A-site deficiency had an opposite effect. The electrochemical impedance spectroscopy studies revealed a rather poor activity of $Sr_{1-x}(Ti,V)O_{3-\delta}$-Ni porous electrodes for hydrogen oxidation reaction. This was ascribed to insufficient intrinsic electrocatalytic activity of $Sr_{1-x}(Ti,V)O_3$ perovskites, low expected ionic conduction in these phases, and segregation of Ni particles in the course of synthesis. It was demonstrated that the electrochemical performance of these electrodes can be substantially improved by the infiltrations of gadolinia-doped ceria as oxygen-ion conducting component and small extra amounts of well-dispersed Ni as an electrocatalyst.

## List of figures

## List of tables

## List of symbols

A – Area

$A_0$ – Pre-exponential factor for conductivity

$E_A$ – Activation energy

I – Current

L – Thickness / Length

M – Molar mass

m – Mass of a sample

n – Number of electrons

$O^{2-}$ – Oxide ion

$pO_2$ – Oxygen partial pressure

R – Ideal gas constant

$R_{ohm}$ – Ohmic resistance

$R_p$ – Polarization resistance

$R_T$ – Total resistance

$r_a$ – Ionic radius of the A-site cation

$r_b$ – Ionic radius of the B-site cation

$r_o$ – Ionic radius of the Oxygen anion

T – Temperature

V – Voltage

$V_O$ – Oxygen vacancy

Z – Impedance

σ – Electrical conductivity

τ – Goldschimdt tolerance factor

## List of abbreviations

EDS – Energy-dispersive X-ray spectroscopy

EIS – Electrochemical impedance spectroscopy

Eq – Equation

Fig – Figure

HEM – High Energy Milling

SEM – Scanning electronic microscopy

SOC – Solid oxide cell

SOEC – Solid oxide electrolysis cell

SOFC – Solid oxide fuel cell

SSR – Solid state reaction

TEC – Thermal expansion coefficient

TPB – Triple-phase boundary

XRD – X-ray diffraction

Of used materials:

STVN – $Sr(Ti,V,Ni)O_3$ composition

CGO – Cerium Gadolinium Oxide

YSZ – Yttria Stabilized Zirconia

# 1. Introduction

## 1.1. Solid oxide fuel and electrolysis cells

A solid oxide cell (SOC) is an electrochemical system comprising dense (physically impermeable) solid electrolyte membrane and two porous electrodes applied onto the opposite sides of the membrane as the main components. The electrolyte is an oxygen-ion- or, less often, proton-conducting oxide ceramic material, whereas the electrodes work as air electrode or fuel electrode. The final device comprises also other components, such as interconnects, housing and sealants. Basically, SOC may operate in one of two modes: a fuel cell mode or an electrolyser mode.[1]

The system operating in the first mode is commonly known as solid oxide fuel cell – SOFC. SOFC is the energy conversion system which produces electricity via electrochemical oxidation of the fuel, which may be of a variety of compositions: $H_2$, natural gas, biogas and syngas. In the course of operation, air is supplied to the porous cathode (air electrode), and fuel is supplied to the porous anode (fuel electrode). Oxygen is reduced electrochemically at the cathode by accepting electrons supplied from an external circuit to form oxygen ions (Eq. 1), which are then transported to the fuel electrode through the ion-conducting electrolyte. At the anode, the oxygen ions combine with $H_2$ and/or CO (as simplest examples of fuels) forming steam and/or $CO_2$ and releasing electrons into external circuit (Eq. 2 and 3) thus generating electric current.[2,3]

$$O_2 + 4e^- \rightarrow 2O^{2-} \quad \text{(Equation 1)}$$

$$2H_2 + 2O^{2-} \rightarrow 4e^- + 2H_2O \quad \text{(Equation 2)}$$

$$2CO + 2O^{2-} \rightarrow 2CO_2 + 4e^- \quad \text{(Equation 3)}$$

In the electrolyser mode, solid oxide electrolyser cell (SOEC), the anode and cathode functions of the electrodes are reversed. This mode is also known as a reverse fuel cell, or regenerative fuel cell, since through the electrolysis of water and/or carbon dioxide, the cell is able to produce hydrogen gas and/or carbon monoxide, respectively, and oxygen, by reducing the feed, resulting in energy from the electron freeing that may be stored.[4] Some interesting scenarios may arise with the use of this configuration; for instance, storage of energy excess is possible in the production of $H_2$.[2] The operating principles of both SOEC and SOFC are illustrated in Fig. 1.1 and can be summarized as conversion methods of

chemical energy to electrical energy or vice versa. The concept of a solid oxide cell operating alternately in the fuel cell and electrolyser modes is called a Reversible Solid Oxide Cell (r-SOC).

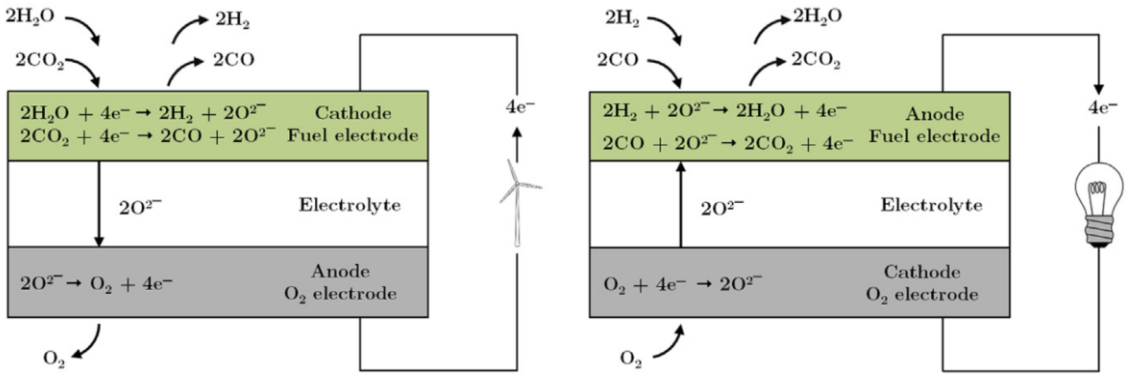


**Figure 1.1: Operating principle of a solid oxide electrolysis cell (SOEC, left) and a solid oxide fuel cell (SOFC, right).[2]**

In terms of cell design, there are two commonly used designs for the stack of a SOFC, as illustrated by Fig. 1.2. The first design is planar, where the cell may assume two variants: a circular disk form, fed with fuel from the central axis, and a square plate fed from the edges. The second design is tubular, and the variable factor is its diameter, going from 15 mm to 5 mm. If the tubes are flat, there is the possibility to join multiples tubes in bundle, in order to deliver higher power density and easier printable surfaces for depositing the electrode layers.[5]

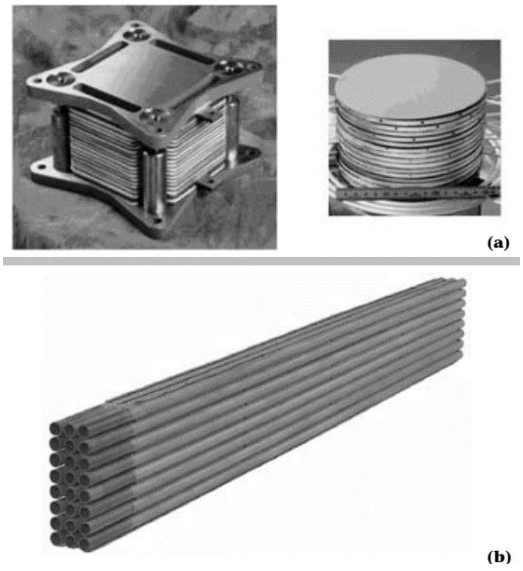


**Figure 1.2: Illustration of planar cell stacks (a) and a tubular cell bundle (b).[4,5]**

Comparing the two, the tubular cell bundle scheme presents advantages over the planar, such as the air and fuel being naturally isolated, with the tubes closed at one end, whereas the planar cell stacks should be provided with an effective seal to isolate them. This seal must have a thermal expansion matching the fuel cell components, be electrically insulating and thermochemically stable under operating conditions. It should also be able to form at low temperatures, enough to avoid damaging the cell components (under 850 °C), while avoiding its migrating/flowing from the designated sealing region, as well as withstand thermal cycling between operation temperature and room temperature. Hence, the performance of planar cell stacks is much more dependent on the successful development of sealing materials. However, if power density is to be compared, the planar design is more desirable, presenting values up to 2 $W.cm^{-2}$ for single cells, and around 0,5 $W.cm^{-2}$ in stack formation, considerably higher than 0.2 $W.cm^{-2}$ for a tubular cell, with volumetric power density following the same trend for both.[5]

## 1.2. Solid oxide cell materials

### 1.2.1. General requirements

When selecting materials for SOC devices, it should always be followed, as good as possible, the following criteria, established in four principles:

- Suitable electrical conducting properties;
- Adequate chemical and structural stability at high temperature for cell operations, but also during the cell fabrication;
- Minimal reactivity and interdiffusion among different components;
- Matching thermal expansion among different components.

A balance must be done between the components of the SOFC. For example, both electrodes should be highly conductive – 100 $S.cm^{-1}$ at working temperature is already considered a good value – but being so without the cost of thermal mismatch, as interface with electrolyte should be preserved.[6] And while the electrolyte should have a large chemical compatibility with other cell materials, its thermochemical expansion should also be suitable and compatible to other components, to allow tolerance to thermal cycling. As for the other minor components – interconnects and sealants – they should follow the stability criteria for the cells, but should also be effective in their functions, which are to conduct the current between electrodes efficiently and ensure sealing within acceptable leakage rates, respectively.[5]

### 1.2.2. Solid electrolytes – a brief overview

Yttria Stabilized Zirconia (YSZ) is regarded as a state-of-the-art electrolyte material for SOFC/SOEC, together with other two: strontium magnesium-doped lanthanum gallate (LSGM) and gadolinium/samarium-doped ceria (CGO or CSO).

YSZ fulfills the electrical requirements above 700 °C and has good high mechanical properties. The first SOFCs based on YSZ electrolytes, operating in the 1990s, had working temperatures around 1000 °C. Such high temperatures facilitated the electrode reactions and promoted fast ionic movement, making the electrochemical reactions faster. On the present, most YSZ-based cells can efficiently operate at around 800 °C, with many alternatives being experimented to operate at even lower operating temperatures. Essentially, lowering the operational temperature is beneficial to the cost for operation, as investment of new materials can be reduced and cell degradation problems (for example, interdiffusion between cell components) be mitigated. However, some disadvantages of lowering the temperature are also to be considered, mainly the slower electrode kinetics and the decrease of available oxide ions, leading to high resistance losses.[7] Main strategies to reduce the operational temperature of SOCs devices without worsening their performance include decrease the thickness of the electrolyte and support the cell on one of the electrodes, the interconnectors or any other external element.[6]

Generally, LSGM and CGO/CSO-based cells can operate efficiently at temperatures around 550 °C. However, LSGM electrolytes are mostly incompatible with the Ni-containing electrodes. On the other hand, CGO-based electrolytes have great functionality when doping with rare earth metals like samarium or gadolinium, but in reducing conditions $Ce^{4+}$ ions may be reduced to $Ce^{3+}$, thus introducing electronic conductivity and causing the cell to be less efficient, especially when reversibility is intended.[5,7]

### 1.2.3. Fuel electrode materials

When it comes to electrode materials, there are more to be considered other than high electrical conductivity and good electrocatalytic activity. Production quality is also an important factor. For instance, processing the set of electrodes as highly porous layers will improve the gas transportation from electrochemically active sites. High specific area, in this case, is responsible to maximize this process. Mixing electronic and ionic transport in the electrode is also another way to improve electrocatalytic activity.

Regarding electrode materials with said characteristics, there are a variety of different compositions that may group onto certain categories. The following sections will describe two main categories of fuel electrode materials currently developed.

### 1.2.3.1. Ni-YSZ cermets

The first SOFCs were based on an electrolyte of YSZ, an anode of Nickel and Yttria Stabilized Zirconia (Ni-YSZ) cermet and a cathode of Lanthanum-Strontium Manganite (LSM). Ni-YSZ cermets have been the most used anode because the comparatively low cost of nickel, good chemical stability and excellent catalytic activity towards hydrogen oxidation. In these materials, the Ni metal phase is responsible for providing a path for electronic conduction and for acting as a catalyst for the electrochemical reaction of fuel oxidation. On the other hand, the YSZ serves to decrease the overall thermal expansion coefficient of the anode to match that of the electrolyte, prevents the Ni phase from coarsening, and offers a conduction path for oxide ions and thus extending the triple phase boundary. The triple phase boundary (or TBP) is a place of a contact of the gas phase (either fuel or oxidant), the electronically conducting phase (electrode) and the ionically conducting phase (solid electrolyte) where an electrochemical reaction actually occurs, in a general case.[8,9] In the case of fuel cells, the three phases are represented by the electrolyte (ion conductor) and both electrodes (electron conductor and fuel transportation).

Despite the great advantages of Ni-YSZ-based SOFCs, they have many drawbacks including carbon deposition and sulfur poisoning that may cause a drastic performance degradation of the cell. Thus, in addition to the catalyst-ability towards fuel oxidation, metallic Ni also favors the formation of carbon deposits when hydrocarbons are used as fuels, causing irreversible damage and degradation of the cell performance (Fig. 1.3). Ni-YSZ cermets have also been reported to be very sensitive to sulfur poisoning, even at very low concentrations. Generally, $H_2S$ reacts with $O_2$, releasing $H_2O$ and S. S may then settle down on the active sites at the operating SOFC temperatures (*e.g.* $Ni_3S_2$ may form by the reaction between Ni and S).[10]

Associated risks to redox cycling and microstructural ageing of Ni-YSZ-based SOCs may cause irreversible anode damage and cell failure by cracking. Fig. 1.4a shows schematically the occurring changes on Ni-YSZ during redox cycling. Furthermore, Fig. 1.5 includes a micrograph or a Ni-YSZ-based cell after degradation caused by re-oxidation.

Lastly, on Fig. 1.4b the microstructural degradation of a cermet Ni/YSZ electrode due to nickel particles agglomeration is schematized.

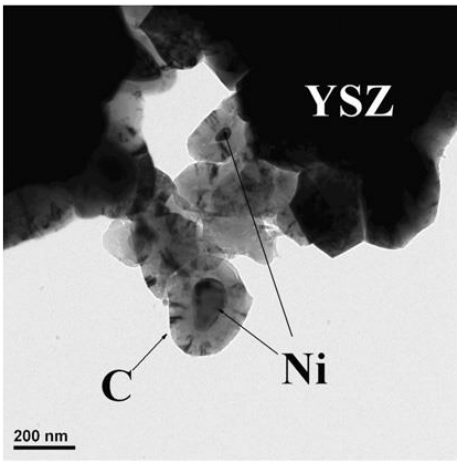


**Figure 1.3: Example of carbon deposition and blocking of Ni catalyst particles in Ni/YSZ cermet anode after operation using hydrocarbon fuel.[11]**

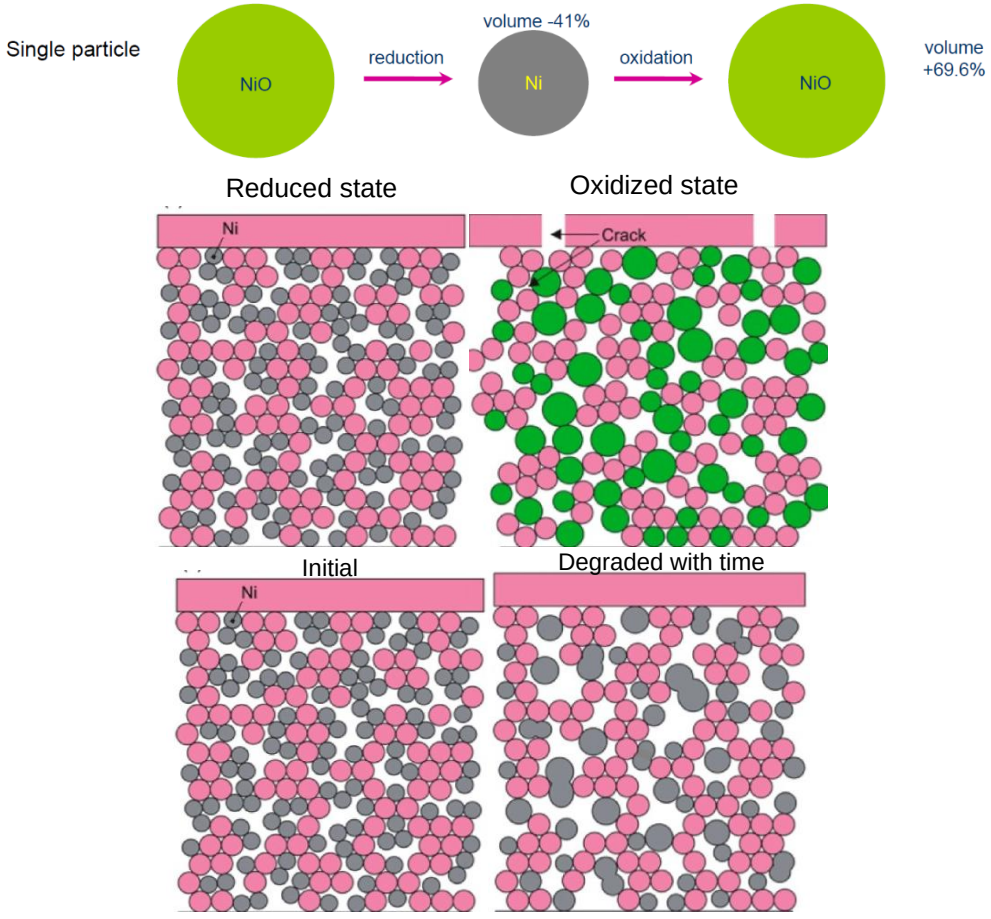


**Figure 1.4: Schematic representation of: Dimensional changes occurring on redox cycling of a Ni-YSZ cermet (a)[11] and microstructural degradation due to Ni agglomeration, leading to broken connection paths and reduced surface area of catalyst (b).[8]**

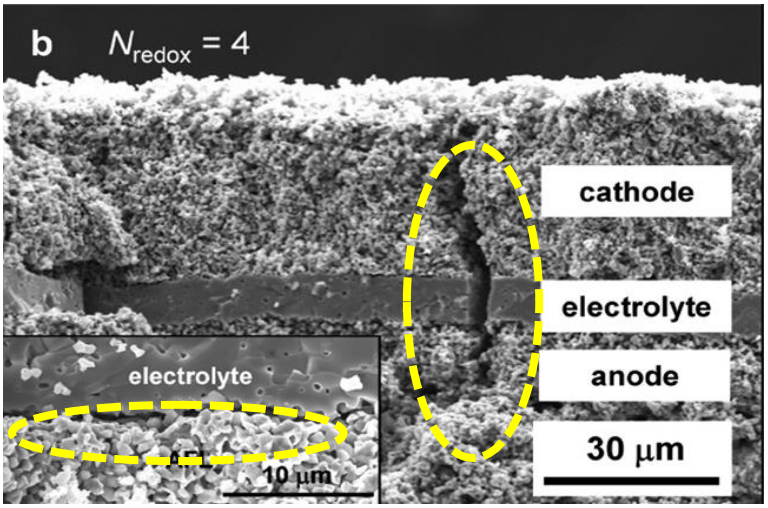


**Figure 1.5: Micrograph or a Ni-YSZ-based cell after degradation caused by re-oxidation.[12]**

### 1.2.3.2. Oxide ceramics – perovskite-like electrodes

The limitations of Ni-YSZ-based cells have led to the development of alternative oxide anode materials. Most oxide materials are electronic conductors (MIEC), having considerable electronic and ionic conductivity. This way, electrochemical oxidation is not confined to TPB, but extends to solid-gas two phase boundaries. Furthermore, they do not suffer from carbon deposition. Apart from the catalytic activities, oxide anode materials should match other requirements, suggested by Steele et al.[13] and listed bellow:

1. Good electronic conductivity (preferably > 100 $S.cm^{-1}$) at anode operating potentials (−0.7 to −0.9 V);

2. Predominant anion lattice disorder to enhance oxygen diffusion coefficients;

3. Good oxygen surface exchange kinetics;

4. Fabrication of porous adherent films with minimal processing problems;

5. Compatibility with solid electrolyte.

Still, there are many subcategories of oxide materials of different characteristics, such as the well documented zirconia/ceria-based fluorites. However, none of which can

cover both functions of anode and cathode simultaneously, apart from some materials with perovskite structure (Fig. 1.6).

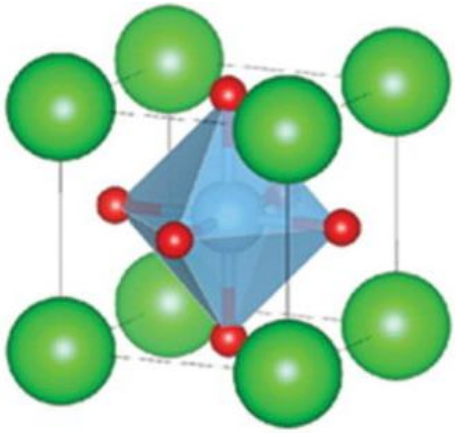

**Figure 1.6: Representation of a perovskite cell; space group 221 (Pm3m).[14]**

A perovskite of general formula $ABO_3$ consists of a cubic unit cell where A atoms (green in Fig. 1.6) sit at the cube corner positions, oxygen atoms at the center of the cube's faces (red in same Fig.) and a single B atom at the body-center position. The structure is considerably adaptable to lattice mismatch between the (A–O) and (B–O) bond lengths and can accommodate more than one A-site and/or B-site cation species. These A and B elements could be, respectively, rare-earth and/or lanthanoid cations and first-row transition metal cations. Particularly, perovskites containing transition metals (e.g. Ti, Nb, V, Mo, etc.) are of interest due to their availability of accommodate multiple oxidation states in function of $p(O_2)$ and therefore the formation of oxygen vacancies under reducing atmospheres, according to Eq. 4.[15]

$$O_O^X \leftrightarrow 2\ e' + \tfrac{1}{2}\ O_2 + V_O^{\cdot\cdot} \qquad \text{(Equation 4)}$$

Apart from transition metal-based perovskites, there are many other perovskite-based materials that are also eligible as potential materials for SOC, but if focusing on the electrodes, not only it is possible to produce a functional SOFC with both electrodes containing transition metal perovskites, but also building a SOEC could be viable, as long as cathode properties are optimized.[14,16]

### 1.2.3.3. $SrVO_{3-\delta}$-based electrode materials

Strontium Vanadate, $SrVO_{3-\delta}$, has arisen as a great alternative as a SOFC anode, and much so due to its great compatibility with hydrocarbon fuels. In its undoped form, $SrVO_3$ exhibits high electronic conductivity under operation conditions, at 1000 $S.cm^{-1}$ for 800°C, with $pO_2$ around $10^{-17}$ atm. Oxygen deficiency values at room temperature of $\delta = 0.1$ are considerable and should imply relatively high ionic conductivity, which contributes to overall electrical conductivity and is favorable for electrocatalytic performance. Furthermore, it presents high tolerance of $H_2S$ in the fuel, for concentrations as high as 10%, and does not catalyze carbon deposition. These are very good properties to have on a SOC electrode, which may lead to very interesting optimization scenarios by doping the oxide, in order to overcome its drawbacks.[17,18,19]

Figure 1.7 presents the $SrO–V_2O_5$ phase diagram, where many Sr-/V- based oxides are included.[20] Accordingly, as $V_2O_5$ content increases resulting secondary phases have lower melting points. Although it is not present in the diagram, the transition of $SrVO_3$ to liquid phase happens in some point above 1869 K. This is the melting point of the secondary phase $Sr_3V_2O_8$ – also written as $Sr_3(VO_4)_2$ – which is a very similar phase to $SrVO_3$ but with modified crystal structure, shifting into a trigonal system.

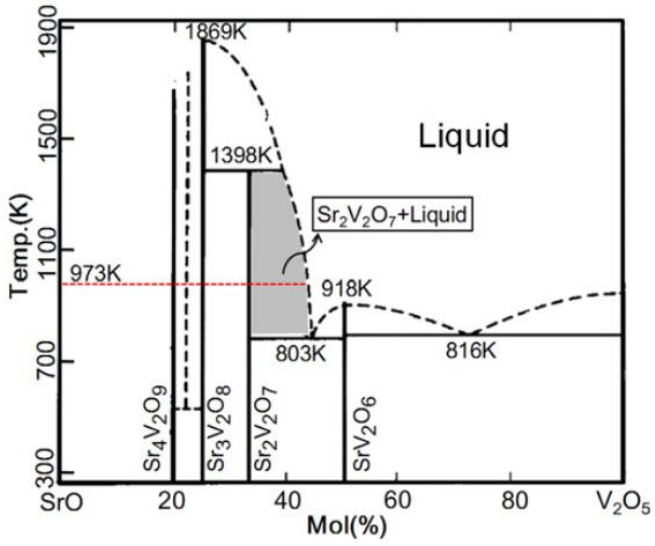


**Figure 1.7: Phase diagram for the $SrO–V_2O_5$ system.**[19]

The major disadvantage of using pure $SrVO_3$ as a SOFC anode is its lattice instability in oxidizing atmospheres. Upper $p(O_2)$ stability boundary was reported to increase to approximately $10^{-15}$ atm at 900 °C, which under oxidizing conditions, makes the

perovskite phase transform into an insulating strontium pyrovanadate, of chemical formula $Sr_2V_2O_7$ (present in figure 1.7). This phase results from the oxidization of $V^{4+}$ ions present in $SrVO_3$ when heated in air, which transform into insolated $V5^+$ ions, dropping quite considerably the electrical conductivity. $Sr_2V_2O_7$, with its low melting point comparable to $SrVO_3$, decomposes quite quickly, and larger lattice parameters, which implicates a volume increasing.[12,21] This, in addition to $SrVO_3$ being a material with a high thermochemical expansion coefficient (TEC = 21.6 × $10^{-6}$ $K^{-1}$ at 823–1273 K), makes the scenario of degradation much more probable along its life cycle.

Reversibility under fuel cell operation conditions is not a certainty, as literature reports are somewhat contradictory on that matter. For example, some reports claim the reduction of $Sr_2V_2O_7$ to $SrVO_3$ is possible at 1000 °C with hydrogen flow [22,23,24], while others indicate that even during exposure to forming gas for 48 hours at 1300 °C, perovskite phase cannot be fully recovered. [25] Adding to that, other intermediate phases such as previously mentioned $Sr_3(VO_4)_2$ were also found in calcinations in $H_2$-containing atmospheres at 1000 °C. All these intermediate phases formed have significantly less electrical conductivity than $SrVO_3$, and contribute to the polarization resistance of the electrolyte, hampering the main reaction of electron transportation even in reducing conditions.

There is a high interest in studying $SrVO_3$-based materials with partial donor-type substitution or doping for use on a SOFC, as they help stabilizing the perovskite phase and maintaining the high standards of conductivity and $H_2S$ tolerance is still achievable. The donor-type substitution occurring for Sr and/or V has the objective of stabilizing the $V^{3+}$ and $V^{4+}$ oxidation state, and to oppose the oxidation to $V^{5+}$ state. Some substitutions may be very appropriate indeed to help shift the Goldschmidt tolerance factor (τ), which is a well-known criterion reflecting the formability and stability of the perovskite lattice. This factor may be determined using equation 5.

$$\tau = \frac{r_A + r_B}{\sqrt{2}\,(r + r_O)} \qquad \text{(Equation 5)}$$

where $R_i$ are the ionic radii of A, B elements and oxygen ions.

Given equation 5, the ideal cubic perovskite structure has a τ of 1. Value which the parent $SrVO_3$ is slightly off: τ = 1.014. Some studies involving the moderate substitution of Sr by rare-earth cations La and Y into the sublattice, with minor co-substitutions by niobium into the vanadium sublattice were successful in approximating this factor to 1 and stabilizing the perovskite. [26] Plus, the inclusion of high amounts of lanthanum in the A-site (~70%) has

been proved to increase the selective oxidation of $H_2S$, with catalytic activity being proportionally direct to the $H_2S$ concentration.[27] For example, Fig. 1.8 shows the effect of the introduction of relatively small amounts of La and Y in the A-site of the perovskite. Accordingly, it is proposed that the incorporation of $Sr^{2+}$ ions onto $La^{3+}$ sites leads to the formation of $V^{4+}$ ions mixed with $V^{3+}$, which is expected to enhance the conductivity of the material.

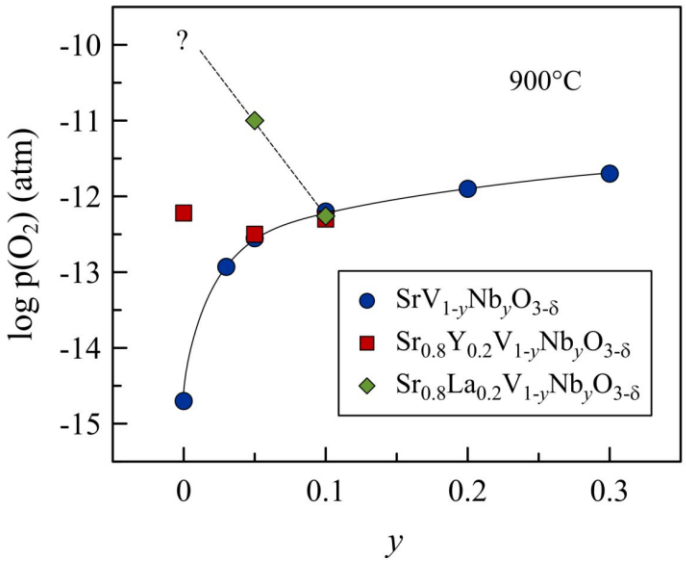


**Figure 1.8: Upper-p($O_2$) stability limits of donor-doped $SrVO_3$ at 900 °C.[20]**

Other perspective to consider in improving the viability of the $SrVO_3$ is, in fact, improving its redox stability, since it will prevent phase transformation. The partial substitution of vanadium with higher-valence transition metal cations, such as $Nb^{5+}$, $Ta^{5+}$, $W^{6+}$ or $Mo^{6+}$, should approximate τ closer to one by increasing the average cationic radius of the B-site species. Also, because these cations have higher valence, the partial reduction from $V^{4+}$ to $V^{3+}$ should be expected.[28] However, this doping mechanism is expected to directly impact the electric conductivity.

As in fact, improving redox stability and reducing conditions would be optimal to fully profit from the use of $SrVO_3$-based electrodes. One other possibility for partial substitution of vanadium, while keeping strontium as first element, would be the choice of a more compatible element to introduce in the B-site. Therefore, following this criterion, a candidate would be strontium titanate, $SrTiO_3$.

### 1.2.3.4. $SrTiO_3$-based materials

Strontium titanate is known to be a ceramic with high phase stability under both oxidizing and reducing conditions. In fact, it has remarkable stability in a wide range of oxygen partial pressure and temperature (800°C, $p(O_2) \approx 10^{-20}$ atm). It has moderate TEC, and its electrical conductivity locates between 0.02 to 0.09 $S.cm^{-1}$ for stoichiometric $SrTiO_3$, being essentially a semiconductor. In its pure state, $SrTiO_3$ is in fact an undesirable option for an electrode material, albeit possessing great stability conditions. Only by reduction at high temperatures its electrical conductivity may increase. Equally to $SrVO_3$, it does not catalyze carbon deposition and it is tolerant to $H_2S$ and derivates.[29]

Addition of other elements to $SrTiO_3$ is also very similar. In terms of strontium sublattice substitution, elements like lanthanum, praseodymium and yttrium were target of study, as well as niobium into the titanium sublattice, for use in SOFC. Although defect chemistry of donor-doped $SrTiO_3$ is not completely established, it is generally accepted that charge compensation for donor additions may be different under oxidizing and reducing conditions. Similarly, the A:B site ratio being slightly shifted from 1:1 may also alter some of the discussed properties. For instance, studies with the inclusion of praseodymium (Pr) in the A-site showed an increase of electronic conductivity in 2 to 3 orders of magnitude with respect to oxidation conditions necessary for SOFC. [30] Fig. 1.9 illustrates this increase both for reducing conditions and oxidized in air.

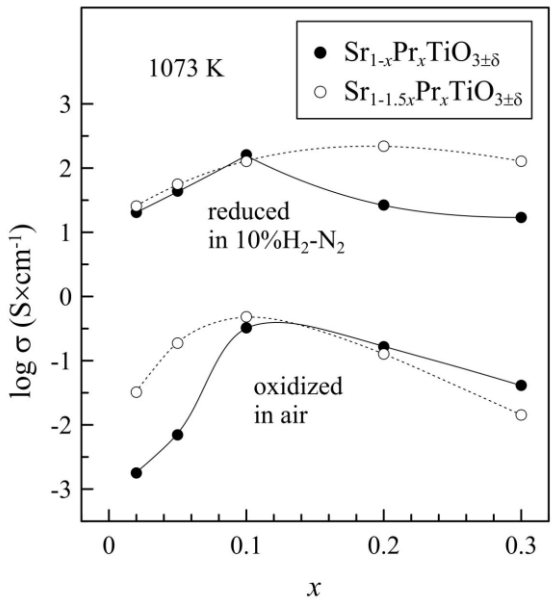


**Figure 1.9: Dependence of electrical conductivity of oxidized and reduced $(Sr,Pr)TiO_{3\pm\delta}$ ceramics on praseodymium content at 800 °C.[22]**

However, one of the most promising possibilities $SrTiO_3$ introduces into the SOC research is the viability of working not only in SOFC, but also in reverse fuel mode, SOEC. And since under oxidizing and reducing conditions it is able to maintain phase stability, system reversibility (*i.e.*, the functions of cathode and anode being reversible) is feasible, meaning the same cell might operate both as SOFC and SOEC effectively. For instance, given a SOEC assembly, a $SrTiO_3$ cathode would be able to generate electrical current through the production of $H_2$ and CO, that would be stored. Reverting this process, $SrTiO_3$ would now be the anode, and since this mode is responsible for energy production, releasing the stored energy back to the system by electrical current could be utilized in multiple ways, such as providing higher energy in high demanding periods.

Remembering that $SrVO_3$ is in fact a fair performer on a SOFC anode, despite its degradation problems, and that $SrTiO_3$ is very stable in both SOC modes, creating a compound of $Sr(Ti,V)O_3$ for SOFC would be conceivable, since both are perovskites of the same structure – which is also their only solid state structure – and have the same substitution compatibilities. Adding to that, both vanadium and titanium, "neighbor" elements in the periodic table, even partly share the same oxidation state. More so, and although exact figures are not available, it is documented that strontium vanadate only achieves its melting point close to 2000°C, similarly to $SrTiO_3$ (2080°C), giving enough margin to compact the crystal lattice at a high temperature. And as recent studies by Macías et al. have shown, there is room to design a $Sr(Ti,V)O_3$ anode. [31,32]

It has been reported that when titanium (0.3-0.5 at.%) is introduced into a $SrVO_3$ (*i.e.* $SrTi_{1-y}V_yO_3$ series) TEC will be noticeable reduced and stability under oxidizing conditions would also significantly improve. Typically, overall conductivity of $y \leq 0.5$ compositions is over 20 $S.cm^{-1}$, which is significantly lower than pure $SrVO_3$ conductivity. Nevertheless, this conductivity values are considered reasonable for SOFC applications. Fig. 1.10 shows the temperature dependence of conductivity for $SrV_{(1-y)}Ti_yO_3$ (y ranged from 0-0.9 at.%) in 10% $H_2$-$N_2$ atmosphere. On the contrary, some secondary phases of vanadate have been detected after testing these materials in oxidizing conditions. This ultimately indicates that when working under anodic polarization the risk of decomposition can not be neglected. At the same time, most of works has reported that when working in inert gas conditions, the secondary phases would not form, which may lead to consider this $SrTi_{1-y}V_yO_3$ series as metastable materials.[24,25]

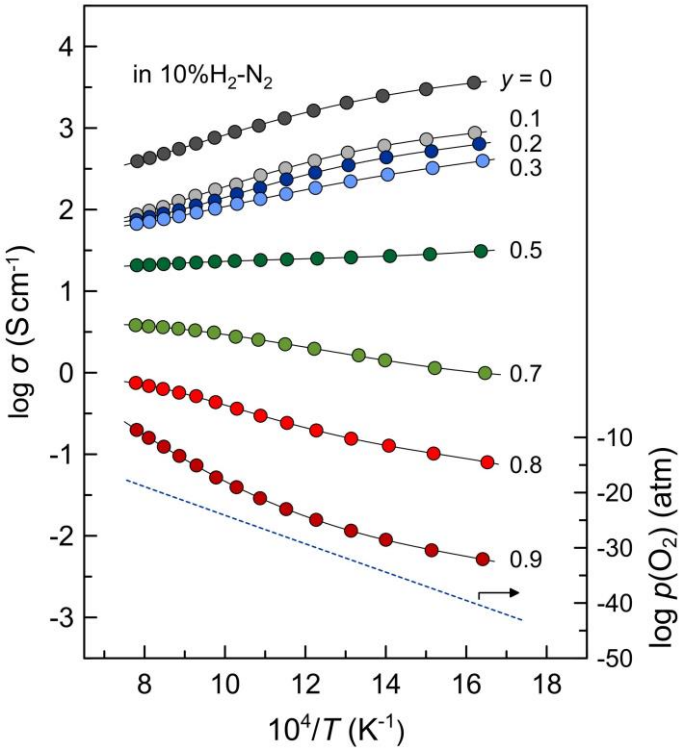


**Figure 1.10: Temperature dependence of electrical conductivity of $SrV_{1-y}Ti_yO_{3-\delta}$ ceramics under reducing atmosphere.[24]**

## 1.3. Electrode Nanostructuring

Realizable performance improvements rely upon strongly-coupled relationships in materials and morphology of electrocatalitically active electrode layers. Althorough conventional composites eectrodes made by mixing ceramic electrolyte and metal (*e.g*. Ni-YSZ cermet)[33] and some mixed ionic electronic conductors (MIECs) can provide electrochemically active surface, their electrochemical activities may not be high enough to obtain a desirable power and work effiently, specially at moderate operation temperatures. this electrochemical activitiy could be improved by nanostructiring the microstructure of the electrode layers, increasing somehow the effective electrode surface area and therefore the concentrtion of active sites in r-SOCs. Lastly, an efficient electrode layer will consists of a porous backbone and an active coating catalyst; the porous backbone providing excellent ionic and electronic conductivity and the infiltrated coating phase possessing high catalytic activity and stability. It has been also theorized that nanosized oxides may enhance the surface vacancy concentration, with positive impact on the electronic and ionic conductivities.[34]

Unlike mixing mixing ceramic electrolyte and Ni metalic in the conventional Ni-YSZ cermets, the process of infiltration is based on the addition of nanoparticles to the internal surface of a porous backbone. This infiltration occurs through a precipitation process of a metal salt containing the catalytic species into the pores of the backbone through a solution, where it later decomposes through firing generating the desired nanoparticulate metallic or oxide catalyst.[35,36] This infiltration method has been reported to enhance the overall cell performance, since the infiltrated nanoparticles act as excellent catalyst, as well as to reduce polarization resistance.[37,38] Fig. 1.11 illustrates how the infiltration process occurs.

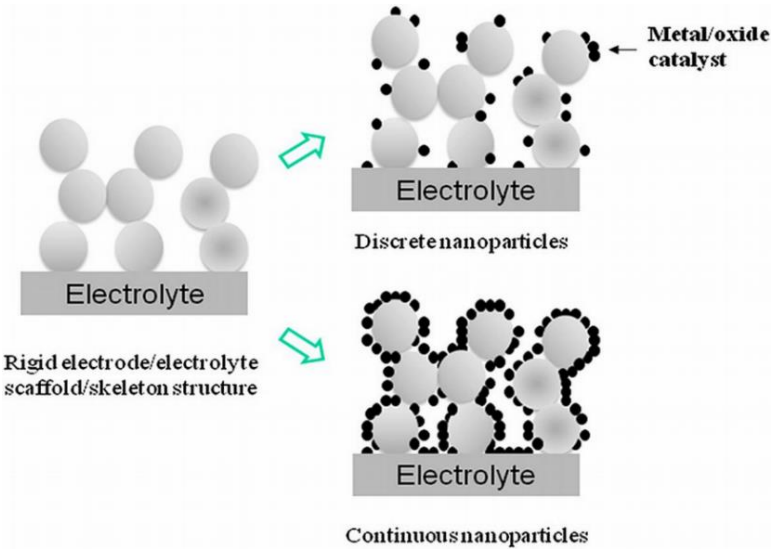


**Figure 1.11: Fabrication of nanostructured electrode via infiltration into pre-sintered porous electrode or electrolyte backbone/skeleton. [38]**

One of the main problems related to infiltration processes, however, has to do with nano-particle distribution. Furthermore, a low concentration of the metal salt in the solution, while optimal for a better control of the impregnation with progressive filling, also requires progressive firing of the sample to achieve intended quantities of catalyst. Even though the firing temperatures of this process are usually lower than the sintering temperatures of the electrodes, it may still lead to electrode degradation and gas diffusion limitations within the electrode, limiting the performance at higher current densities. More so, if the metal salt is more concentrated, requiring less solution to impregnate, reducing the number of firings this way, it may cause pore filling besides the intended coating of pore walls. Although prospects using this infiltration technique are promising, there are still some doubts related to mass production and quality control.

Both direct mixing and infiltration rely on the introduction of a metal/oxide catalyst at different stages of the production of the electrode layers. However, more recent approaches focus on the exsolution, where active metallic phases contained in the B position of an $ABO_3$ perovskite is exsolved (*i.e.*, separated) from the crystal lattice.[39] Fig. 1.12 shows a schematic representation of the exsolution process occurring on a perovskite.

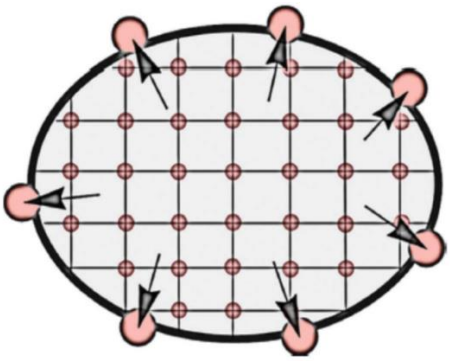

**Figure 1.12: Schematic representation of the exsolution in a perovskite.[40]**

The main advantage of ex-solution over the infiltration process is the durability of the electrode. Theoretically, the exsolution already produces a dispersion of nanoparticles firmly anchored to grain surface, which will minimize the agglomeration of infiltrated nanoparticles with the ageing of the electrode layers. Other than that, results comparing these two techniques are slightly more favorable to the infiltration process.[41] On a positive note, these are not mutually exclusive techniques, meaning that both may be utilized at the same cell, and given the less propensity of nanoparticles agglomeration with exsolution, it may also imply a smaller need to use larger amounts of impregnation or simply a longer service life. Some studies on the matter proved successful on incorporating both techniques together, with further promising results.[42] Lastly, it is worth to mention that A-site deficiency has been suggested to be a key force to trigger B-site cations exsolution,[43,44] which reverts the A-site-deficient perovskite towards a more stable stoichiometric structure.

## 1.4. Objectives of this work

The main objective of this work was to assess the possibility of the enhancement of the electrocatalytic activity of $Sr(Ti,V)O_{3-\delta}$ fuel electrode components by introducing Ni into the

B-sublattice of the perovskite structure with in-situ nanostructuring under operation conditions by exsolution. The particular objectives included:

1. to prepare the series of $Sr1_{-x}Ti_{1-y-z}V_yNi_zO_{3-\delta}$ employing room-temperature high-energy mechanochemical route in combination with thermal treatments under controlled redox conditions;

2. to assess the effects of cation composition and synthetic procedure parameters on the phase formation;

3. to study the electrical properties of prepared ceramic materials and their thermomechanical compatibility with solid electrolytes;

4. to fabricate electrochemical cells with $Sr(Ti,V.Nb)O_3$ electrodes and to assess the possibility of nanostructuring of the electrocatalyst surface;

5. to evaluate the electrochemical performance of selected $Sr(Ti,V.Nb)O_3$-based electrodes.

# 2. Methodology

## 2.1. Selection of ceramic compositions

Based on previous works of Macías et al.,[31,32] $Sr(Ti,V,Ni)O_{3-\delta}$-based compositions were selected according to the Taguchi planning summarized on Table 2.1. Generally, the number of samples in a Taguchi planning are determined by the number of variables, *v*, and the number of levels, *n*, in which *n* is the number of values attributable to each variable. Thus, the number of samples should be, at most, $n^v$. In this work, it will be used three levels (*n* = 1, 2, 3) for each variable (*x, y, z),* giving a total of 81 combinations. However, if relying on planned distributions of low, intermediate and high levels, and selecting one combination instead of all similar nine distributions, the number of combinations can be reduced to nine. Using a correlation matrix, obtained by a least square fitting for each variable, and choosing appropriate levels from literature knowledge, will determine if the chosen levels present a good fitting of an expected result. If the chosen levels are presented as viable, it means the nine combinations of (x, y, z) can be put into samples. All nine compositions ultimately chosen for this work are listed on Table 2.2.

**Table 2.1: Taguchi planning for $Sr_{1-x}Ti_{1-y(1+w)}V_yNi_{yw}O_{3-\delta}$ (STVN) series.**

| $Sr_{1-x}Ti_{1-y(1+w)}V_yNi_{yw}O_{3-\delta}$ | | | |
|---|---|---|---|
| **Level, *n*** | **Variable, *v*** | | |
| | ***x*** | ***y*** | ***w*** |
| **1** | 0 | 0.2 | 0.1 |
| **2** | 0.02 | 0.3 | 0.2 |
| **3** | 0.04 | 0.4 | 0.3 |

**Table 2.2: Synthetized STVN compositions**

| **Variable, *v*** | | | **Nominal composition** | **Abbreviation** |
|---|---|---|---|---|
| **x** | **y** | **w** | | |
| 0 | 0.2 | 0.1 | $SrTi_{0.78}V_{0.2}Ni_{0.02}O_{3-\delta}$ | SV20N2 |
| 0 | 0.3 | 0.2 | $SrTi_{0.64}V_{0.3}Ni_{0.06}O_{3-\delta}$ | SV30N6 |
| 0 | 0.4 | 0.3 | $SrTi_{0.48}V_{0.4}Ni_{0.12}O_{3-\delta}$ | SV40N12 |
| 0.02 | 0.2 | 0.2 | $Sr_{0.98}Ti_{0.76}V_{0.2}Ni_{0.04}O_{3-\delta}$ | S98V20N4 |
| 0.02 | 0.3 | 0.3 | $Sr_{0.98}Ti_{0.61}V_{0.3}Ni_{0.09}O_{3-\delta}$ | S98V30N9 |
| 0.02 | 0.4 | 0.1 | $Sr_{0.98}Ti_{0.56}V_{0.4}Ni_{0.04}O_{3-\delta}$ | S98V20N4 |
| 0.04 | 0.2 | 0.3 | $Sr_{0.96}Ti_{0.74}V_{0.2}Ni_{0.06}O_{3-\delta}$ | S96V20N6 |
| 0.04 | 0.3 | 0.1 | $Sr_{0.96}Ti_{0.67}V_{0.3}Ni_{0.03}O_{3-\delta}$ | S96V30N3 |
| 0.04 | 0.4 | 0.2 | $Sr_{0.96}Ti_{0.52}V_{0.4}Ni_{0.08}O_{3-\delta}$ | S96V40N8 |

## 2.2. Ceramic synthesis and processing

Figure 2.1 shows a schematic representation of the experimental procedure. All proposed ceramic compositions were prepared through solid-state reaction route (Eq. 6) using stoichiometric mixtures of high purity carbonates and oxides as starting reagents: Strontium carbonate ($SrCO_3$, *Sigma Aldrich*, >99.9 %); titanium(IV) oxide, anatase ($TiO_3$, *Sigma Aldrich*, >99.9 %); vanadium(III) oxide ($V_2O_3$, *Sigma Aldrich*, >99.9 %) and nickel oxide (NiO, *Sigma Aldrich*, >99.9 %).

$$(1-x)\,SrCO_3 + (1-y-yw)\,TiO_2 + \left(\frac{y}{2}\right)V_2O_3 + (yw)\,NiO \rightarrow Sr_{1-x}Ti_{1-y-yw}V_yNi_{yw}O_{3-\delta}$$

(Equation 6)

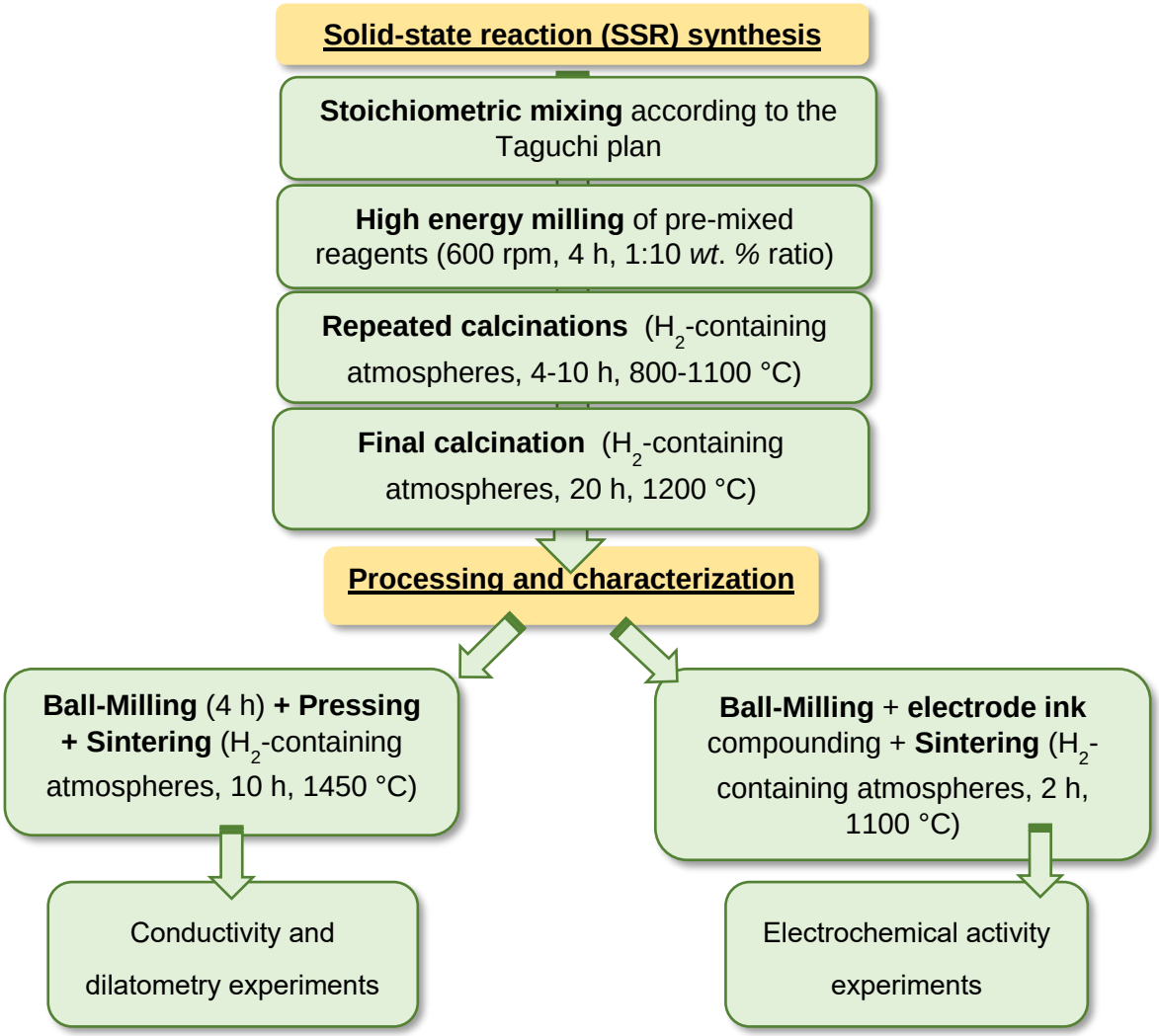


**Figure 2.1: Experimental procedure for the synthesis and the processing of the $Sr(Ti,V,Ni)O_{3-\delta}$-based compositions**

For each composition, a mixture of starting reagents (*ca.* 10 g) were mechanically activated during 4 h in a high-energy planetary ball mill Retsch PM 200. A grinding jar (250 25 0mL in volume) and zirconia balls (10 mm in diameter) were used. The ball-to-powder weight ratio was 10:1. Milling experiments were performed in dry conditions at 600 rpm; using a milling sequence of 5 min clockwise, 5 min pause, 5 min milling counterclockwise. To assess the effect of temperature on the phase formation, activated mixtures were calcinated in $H_2$-containing atmospheres for 4 h at 800, 900 and 1000 °C using a 5 °C/min heating/cooling rate. Equally, the influence of repeated thermal treatments in $H_2$-containing atmospheres (for 4-10 h, up to 1100 °C, $\Delta$ = 100 °C, 5°C/min heating/cooling rate) with intermediate regrinding in ethanol using an agate mortar was also studied.

Selected single phase compositions were ball-milled in ethanol with zirconia balls (diameter = 10 mm) for 4 hours using a Retsch PM200, and then dried for at least 20 hours. Subsequently, ceramic powders were pressed into disks (*ca.* 20 mm of nominal diameter and 2 mm of thickness) and sintered at 1450 °C for 10 hours a $H_2$-containing atmosphere. Final ceramics parts were cut into bar-shaped samples to further proceed with microstructural, dilatometric and electrical characterization.

## 2.3. X-Ray Diffraction

X-Ray Diffraction (XRD) technique was used to monitor the amorphization and the traces of reaction after HEM processes of the pre-mixed starting reagents; as well as to analyze the effect of temperature and repeated thermal treatments in $H_2$-containing atmospheres referred in the section above.

All XRD experiments were performed on crushed powders using a PANalytical X'pert PRO diffractometer (Cu Kα; λ=0.154178 nm; 10-80°, 0.02° step, exposition time of 5 seconds maximum). Phase identification was made using JCPDS database (International Centre for Diffraction Data). Crystal lattice parameters were calculated using FullProf software. [45]Theoretical density was calculated using Equation 7:

$$D_{theor} = \frac{n_U M}{N_A V} \qquad \text{(Equation 7)}$$

Where $n_U$ represents the number of formula units per unit cell and $V$ the volume of the unit cell, $M$ represents molar weight and $N_A$ is the Avogadro constant.

## 2.4. Microstructural characterization

Microstructural characterization of the processed ceramics parts was performed using a Scanning Electron SU-70 Microscope (SEM), coupled with Bruker Quantax 400 detectors for Energy Dispersive Spectroscopy (EDS) analyses. Samples were glued into metallic holders using conductive carbon cement (Wetzlar). Subsequently, a uniform carbon powder layer was sputtered over the samples using a Emitech K950x turbo evaporator.

SEM/EDS studies were also conducted to assess microstructural features; such as electrode layer thickness and morphology, possible interactions between electrolyte and electrode layers or cation interdiffusion, after the electrochemical tests. In these cases, half-symmetrical cells were vertically glued into the metallic holders to focus on the interface between the electrolyte and electrode layer.

## 2.5. Thermal analysis – Dilatometry

Dimensional changes of ceramic bars on thermal cycling (heating/cooling) were determined by controlled-atmosphere dilatometry. These experiments were conducted in a vertical dilatometer Linseis L70 with a constant heating-cooling rate of 3 °C/min from 25 to 1100 °C in $H_2$-cointaining atmosphere. Calibration of the dilatometer was carried out using a $Al_2O_3$ bar. Thermal expansion coefficients (TECs) were calculated from dilatometric curves via a least-square method. Assuming a linear regression, TEC (α) may be calculated through equation 8.

$$\frac{\Delta L}{L_0} = \alpha \Delta T \qquad \text{(Equation 8)}$$

## 2.6. Electrical conductivity

Total conductivity of the ceramics was studied as a function of temperature (T) from 300 to 1000 °C and oxygen partial pressure ($pO_2$) under reducing conditions (air flow introduced in 10% $H_2$-$N_2$ atmosphere, $pO_2$ ranging from $10^{-19}$ to $10^{-5}$ Pa) by means of standard four-probe DC technique. Compare to two-probe methods, by means of four-probe DC technique it is possible to suppress the influence of wires resistance, since current is passed between two outside probes while potential is measured by two inside probes. Figure 2.2 shows a representative scheme of this configuration.

The setup designed to perform the four-probe experiments consisted of a vertical furnace equipped with S-type (Pt/Rh 90%/10%-Pt) thermocouples and an yttria-stabilized zirconia solid-electrolyte sensor for p($O_2$) monitoring. Electrical measurements were obtained using a Yokogawa 7651 power supply and an Agilent 34460A multimeter (equilibration time before each measurement was at least 30 minutes). Ceramic bar-shaped samples were placed inside the furnace and connected using two pairs of Pt wires, one carrying the current and the other sensing the voltage in the bar. End-face surfaces of the bars were additionally covered with Pt paint (Heraeus CL11-5349) to improve electrical contact. Total conductivity was calculated according to Equation 9, which obeys to Ohm's law.

$$\sigma = \frac{I_1+I_2}{V_1+V_2} \cdot \frac{l}{S} \qquad \text{(Equation 9)}$$

Where *l* is the distance between voltage sensing probes, *S* is the cross area, $V_1$, $V_2$ and $I_1$, $I_2$ pairs are, respectively, voltage drop over the sample and current for both current directions.

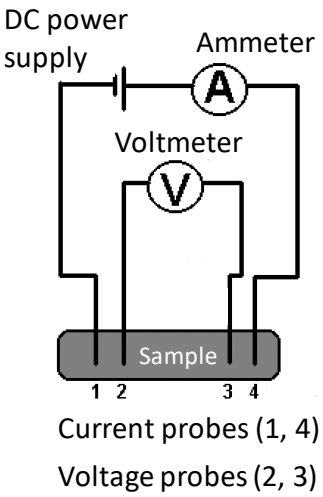


**Figure 2.2. Schematic representation of the four-probe DC technique**

Activation energy was calculated following the Arrhenius equation, expressed in Equation 10.

$$\sigma = \frac{A_0}{T} e^{-\frac{E_A}{RT}} \qquad \text{(Equation 10)}$$

Where $A_0$ is a pre-exponential factor for conductivity, R the ideal gas constant and $E_A$ the pretended activation energy.

Making a linearization in order to obtain $E_A$ with the slope value, as well as $A_0$ in the b coefficient, knowing both conductivity and temperature values, the resulting equation (Eq. 11) is as follows:

$$\ln \sigma T = -\frac{E_A}{R}\frac{1}{T} + \ln A_0 \qquad \text{(Equation 11)}$$

## 2.7. Electrochemical studies

### 2.7.1. Electrode preparation

The electrochemical activity of the $Sr(Ti,V,Ni)O_{3-\delta}$-based electrode layers was studied by Electrochemical Impedance Spectroscopy (EIS) using a AUTOLAB PGSTAT 302 potentiostat/galvanostat (50 mV AC amplitude signal, frequency interval between 1 MHz and 0.01 Hz) equipped with a frequency response analyzer (FRA2) module. The measurements were carried out at 900-700 °C (50 °C step) under zero-current conditions (OCV; Open Circuit Voltage). All the tests started by heating the system up to 900 °C under wet 10% $H_2$-$N_2$ atmosphere, with a heating rate of 3 °C/min followed by 15 to 20 h of stabilization time. Impedance spectra under zero-current conditions were recorded in cooling regime after at least 1 h of stabilization at each temperature.

Samples for electrochemical characterization were based on standard 2-electrode cells in symmetrical configuration (Figure 2.3). Pt paint (Heraeus CL11-5349) was used as counter and reference electrode, and Pt gauzes and Pt wires as current collectors. Solid electrolytes (circa 15 mm of diameter and circa 1.3 mm of thickness) were prepared using commercial $(ZrO_2)_{0.92}(Y_2O_3)_{0.08}$ (YSZ, Tosoh Corp., ≥99.9%) powders sintered in air at 1600 °C/10 hours. Electrode inks were compounded using a 30 % vol. of electrode material and a solution containing α-terpineol (solvent, 30 vol.%), ethyl cellulose (binder, 5 wt.%) and stearic acid (dispersant, 3 wt.%). All components were blended for 4 hours with using a planetary ball-mill and zirconia balls (10 mm in diameter). Final porous electrode layers with an active nominal area of 0.2 $cm^2$ (5 mm in diameter) were brush-painted onto both sides of YSZ solid electrolyte pellets and sintered in $H_2$-containing atmospheres at 1100 °C for 2h using a heating/cooling rate of 3 °C/min.

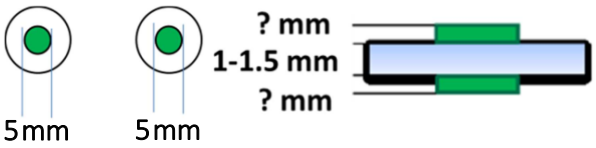


**Figure 2.3. Schematic representation of symmetrical cells, in top view of both sides (left) and in cross section (right).**

All EIS spectra were fitted using equivalent circuits (Figure 2.4) consisting of an inductance (L) element in series with an ohmic resistance ($R_{ohm}$) and two low-frequency (R-CPE) contributions. Specific Polarization resistance, $R_p$, was determined by subtracting the ohmic resistance from the total resistance, dividing it by 2, as they are two electrodes, and multiplying with the surface area. As it is the inverse of conductivity, we can rewrite the Arrehnius equation (Eq. 10) as:

$$\frac{1}{R_p} = \frac{A_0}{T} e^{-\frac{E_A}{RT}} \quad \text{(Equation 12)}$$

Following the same development as before, we may develop equation 12 into:

$$\ln \frac{T}{R_p} = -\frac{E_A}{R}\frac{1}{T} + \ln A_0 \quad \text{(Equation 13)}$$

This way, we may also calculate the activation energy of the cells in function of the specific polarization resistance, $R_p$, and temperature, T.

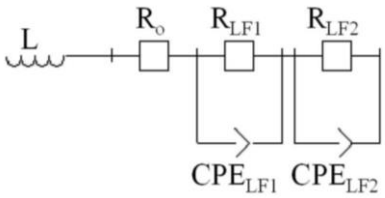


**Figure 2.4. Representative equivalent circuit used to fit the experimental EIS data.**

### 2.7.2. CGO, CGO + Ni infiltration

To investigate the effect of the addition of Gadolinium Doped Ceria (CGO) and Ni on the electrocatalytic activity of porous electrode layers, several aqueous solutions containing ceria nitrate, $Ce(NO_3)_3 \cdot 6H_2O$ (Sigma-Aldrich, ≥99.9%), gadolinium nitrate, $Gd(NO_3)_3 \cdot 6H_2O$ (Alfa Aesar, ≥99.9%) and nickel nitrate $Ni(NO_3)_2 \cdot 6H_2O$ (Sigma-Aldrich, ≥99.9%) were infiltrated onto the electrode layers. Thermal treatment to decompose nitrates

and obtain uniformly dispersed particles Ni and/or CGO particles on the surface of the electrode backbones were performed at 900°C for 2h in $H_2$-cointaining atmospheres. Table 2.3 summarizes the composition of the prepared aqueous solutions. Ni and/or CGO loadings were estimated by measuring the weight before and after the infiltration process. Infiltration process was repeated several times until up to ≈20 wt.% of CGO/CGO:Ni. Figure 2.5 illustrates this infiltration procedure.

**Table 2.3: Infiltration solutions, concentrations and treatment**

| Solutions | Infiltrations (molar ratio) | | | Infiltration treatment |
|---|---|---|---|---|
| | CGO | CGO:Ni | | |
| $Ce(NO_3)_3 \cdot 6H_2O$ | 9 | 9 | 9 | 900 °C, 2 hours, 3 °C/min, in 10% $H_2$-$N_2$ atmosphere |
| $Gd(NO_3)_3 \cdot 6H_2O$ | 1 | 1 | 1 | |
| $Ni(NO_3)_2 \cdot 6H_2O$ | - | 1 | 5 | |

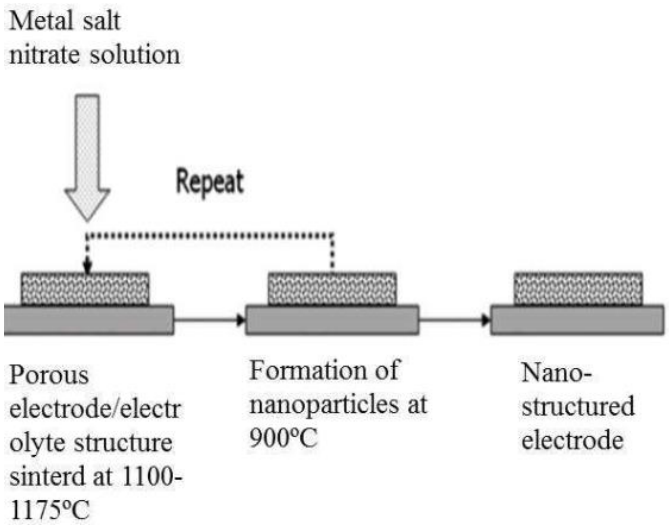


**Figure 2.5. Typical process for the infiltration of metal salt nitrate solution into a pre-sintered electrode porous structure.[46]**

# 3. Results and discussion

## 3.1. Synthesis and phase evolution

### 3.1.1. Effect of mechanochemical treatment

Before starting the synthesis, all as-mixed precursors were submitted to XRD analysis for comparative purpose. The recorded patterns showed the presence solely of the peaks of initial reagents, in agreement with the ICDD PDF database. Fig. 3.1 compares XRD patterns of the precursor mixtures for the selected compositions before and after mechanochemical treatment. It was found that HEM during 4 h results mainly in decreasing intensity and broadening of all reflections, most likely, caused by the decrease in particle size, by the lattice strain induced by high-energy milling, and possibly even by a partial amorphization of initial phases. An onset of $SrTiO_3$-based cubic perovskite phase was observed in some cases; one example is S96V30N3 (Fig.3.1). However, the intensity of reflections of this phase was still low after 4 h of intensive milling. It was decided, therefore, to proceed with the thermal treatments in order to avoid possible contaminations of the precursors my milling media material ($ZrO_2$) in the course of longer HEM. Even though the mechanochemical treatment had a weaker effect in terms of phase formation than it was expected, it certainly provided a good homogenization of the precursor mixtures favorable for further synthetic procedure.

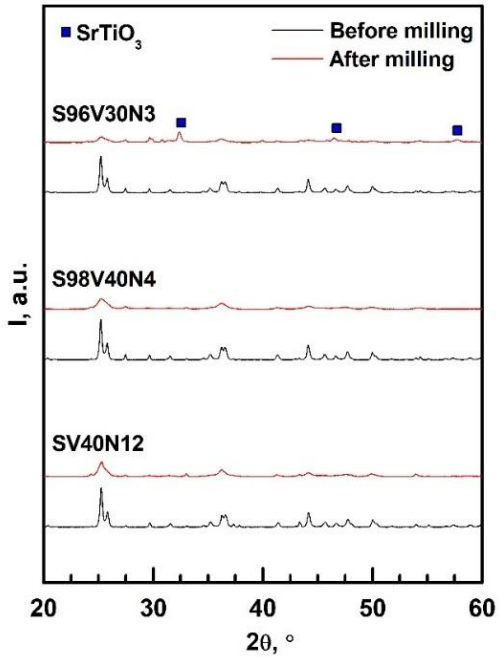


**Figure 3.1: Examples of XRD patterns of the precursor mixtures before and after mechanical treatment (4 h, 600 rpm). Unmarked peaks correspond to the initial reagents.**

### 3.1.2. Effect of temperature in the phase formation

Ideally, the thermal treatment temperature should be high enough to promote the formation of desired phase, but at the same time as low as possible to avoid the agglomeration of particles, especially Ni particles. Therefore, the first calcination of pelletized mechanochemically-activated precursors was performed at 800 °C during 4 h. The corresponding XRD patterns are given in Fig. 3.2. The results showed formation of $SrTiO_3$-based cubic perovskite as main phase, in most cases. At the same time, XRD patterns revealed the presence of substantial number of other phases, including vanadium-based $Sr_3(VO_4)_2$ and $Sr_{10}V_6O_{25}$, metallic Ni, and traces of unreacted $TiO_2$. Thus, temperature of 800 °C was not high enough to promote the preferential formation of desired cubic perovskite phase.

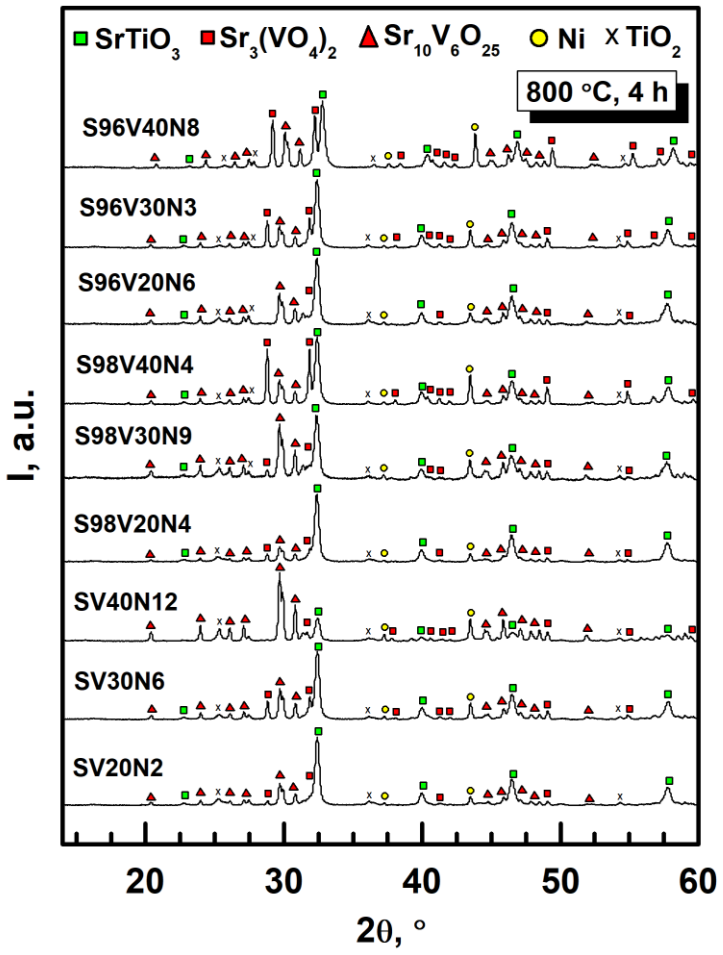


**Figure 3.2: XRD patterns of the samples sintered at 800 °C for 4 h.**

Fresh pelletized samples made of mechanochemically-activated precursor mixtures were therefore sintered at higher temperatures – 900 °C and 1000 °C – for the same period of time (4 h) to check the effect of temperature on the phase formation. The XRD patterns recorded after the sintering steps are presented in Figs. 3.3 and 3.5; Figs. 3.4 and 3.6 shows the corresponding fractions of different phases estimated using semiquantification method in X'Pert Highscore Plus software.

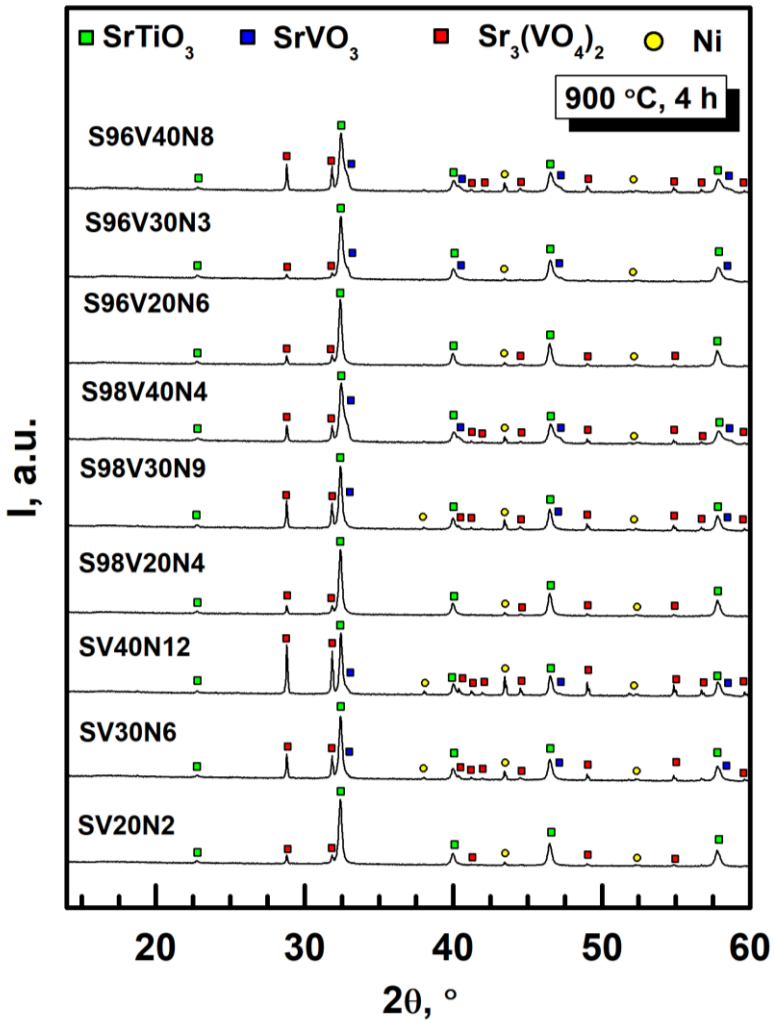


**Figure 3.3: XRD patterns of the samples sintered at 900 °C for 4 h.**

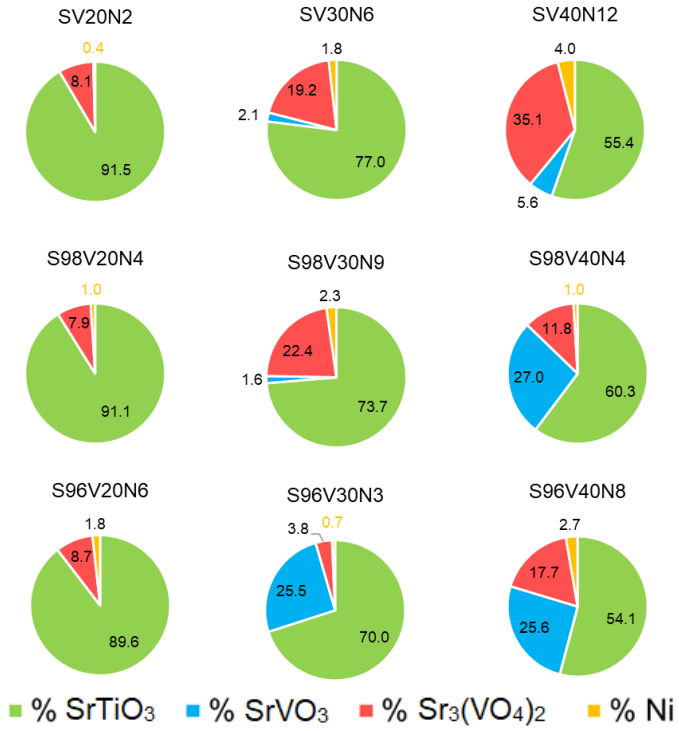


**Figure 3.4: Estimated fractions of different phases in the samples sintered at 900 °C for 4 h.**

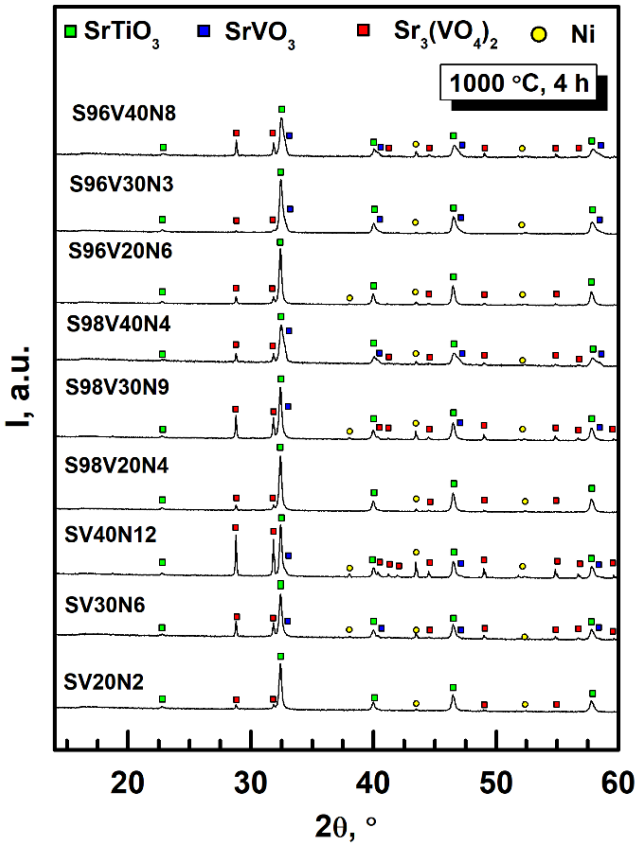


**Figure 3.5: XRD patterns of the samples sintered at 1000 °C for 4 h.**

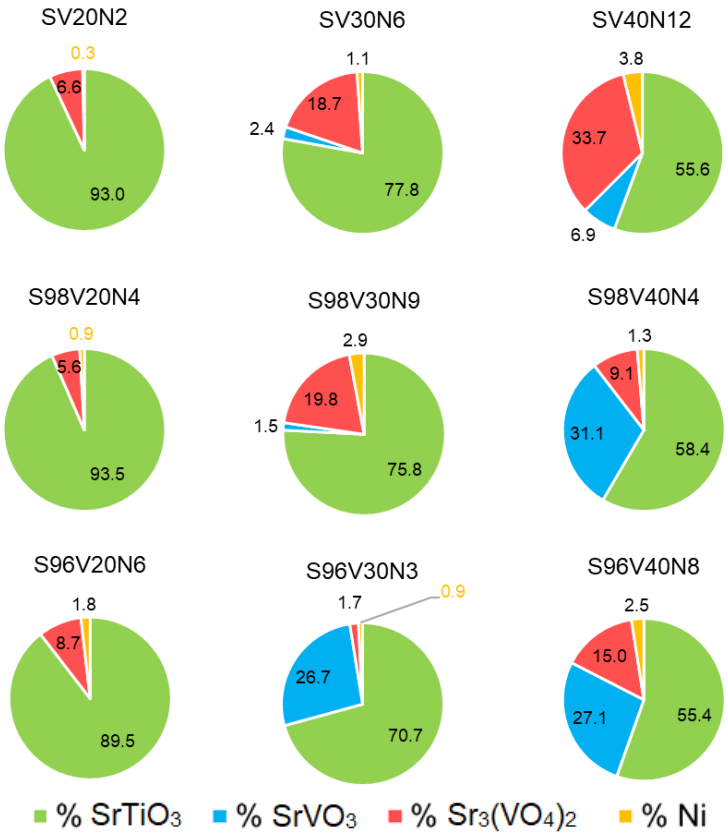


**Figure 3.6: Estimated fractions of different phases in the samples sintered at 1000 °C for 4 h.**

Increasing temperature of thermal treatment from 800 °C to 900-1000 °C promoted the formation of desired $SrTiO_3$-based cubic perovskite phase, which was a major phase for all compositions. Three additional phases were detected in all XRD patterns. The fraction of metallic Ni phase in the samples reasonably varied according to the nominal nickel content. The content of strontium orthovanadate $Sr_3(VO_4)_2$ varied strongly with the total composition, from ~4 to 35 wt. % (for the sample sintered at 900 °C). Additionally, the presence of second cubic perovskite phase based on $SrVO_3$ was detected in XRD patterns of most samples. The lattice parameters of two perovskite phases are close to each other, leading to substantial overlapping of their reflections. Rising sintering temperature from 900 to 1000 °C yielded qualitatively similar results with only a minor decrease in the fraction of $Sr_3(VO_4)_2$ phase impurity. Before further increasing the firing temperature until single-phase would be achieved, it was tested the effect of consecutive firings in two compositions and if single-phase would be achievable this way.

### 3.1.3. Phase evolution in consecutive thermal treatment steps

As the short-term calcinations at 800-1000 °C were not efficient to obtain the desired single-phase perovskite materials, the next step was to assess the evolution of the phase composition in consecutive firing steps of pelletized samples while increasing temperature from 800 to 1100 °C and then time at 1100 °C, as illustrated in Fig. 3.7. The pellets were crashed after each thermal treatment step, and a small sample of the powdered pellet was used to collect the XRD pattern. The rest of the powder was pelletized again and subjected to the next thermal treatment step. Two different nominal compositions were selected for these experiments – one with a higher nickel content and without A-site vacancies (SV40N12), and second with a low nickel content and higher nominal concentration of vacancies in the Sr sublattice (S96V30N3). The results are presented in Figs. 3.8-3.11.

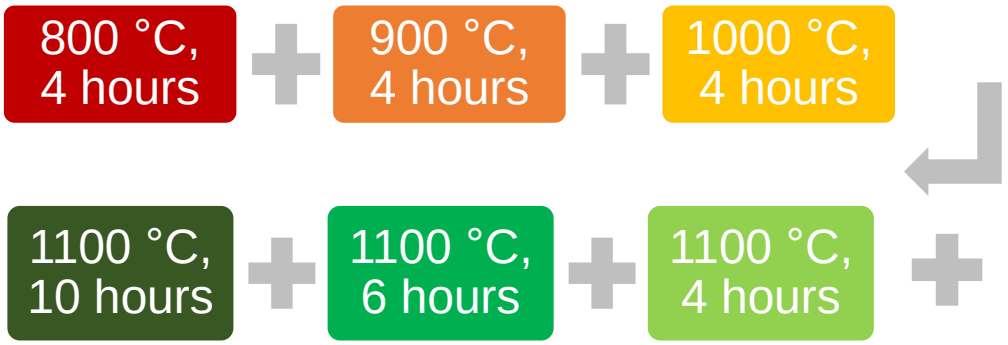


**Figure 3.7: Scheme of the consecutive thermal treatments**

The results of XRD analysis of the samples after the treatments at lower temperatures (800-900 °C) were qualitatively similar to that discussed in subsection 3.1.2. In the case of SV40N12, subsequent firing at 1000 and 1100 °C did not result in noticeable improvements. The sample still contained large fractions of strontium orthovanadate (~30-33 wt. %) and second perovskite-type phase in addition to the main $SrTiO_3$-based perovskite and a fraction of metallic nickel. The contents of undesired $Sr_3(VO_4)_2$ started to decrease slowly with increasing treatment time at 1100 °C (Fig. 3.9).

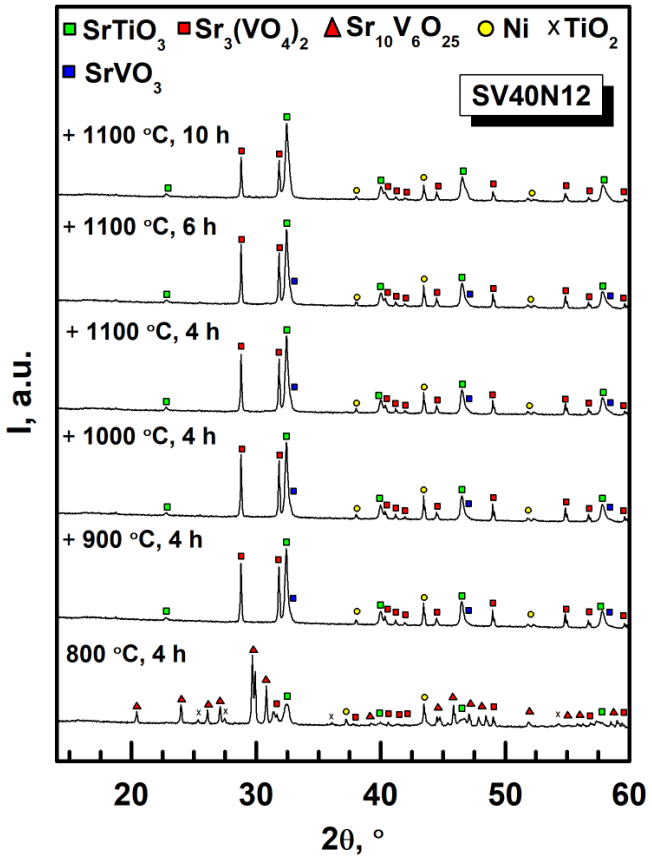


**Figure 3.8: XRD patterns of SV40N12 after consecutive thermal treatment steps (from bottom up) at 800-1100 °C.**

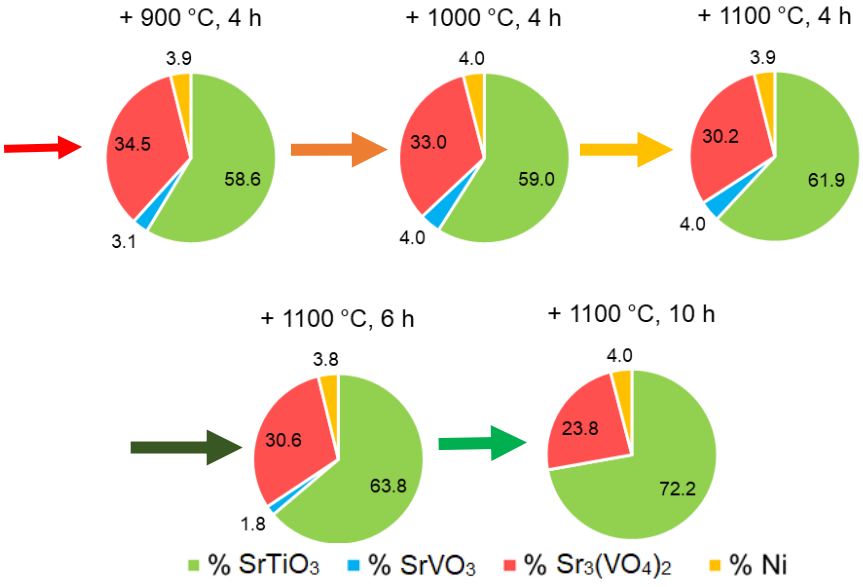


**Figure 3.9: Estimated fractions of different phases in SV40N12 sample after consecutive firing steps at 900-1100 °C.**

On the contrary, S96V30N3 sample contained only trace amount of $Sr_3(VO_4)_2$ impurity after thermal treatment step at 1000 °C (Figs. 3.8 and 3.9). This secondary phase disappears after calcination at 1100 °C, although the second perovskite phase is still present even after longer firing at this temperature, as indicated by asymmetry of reflections of the main perovskite phase.

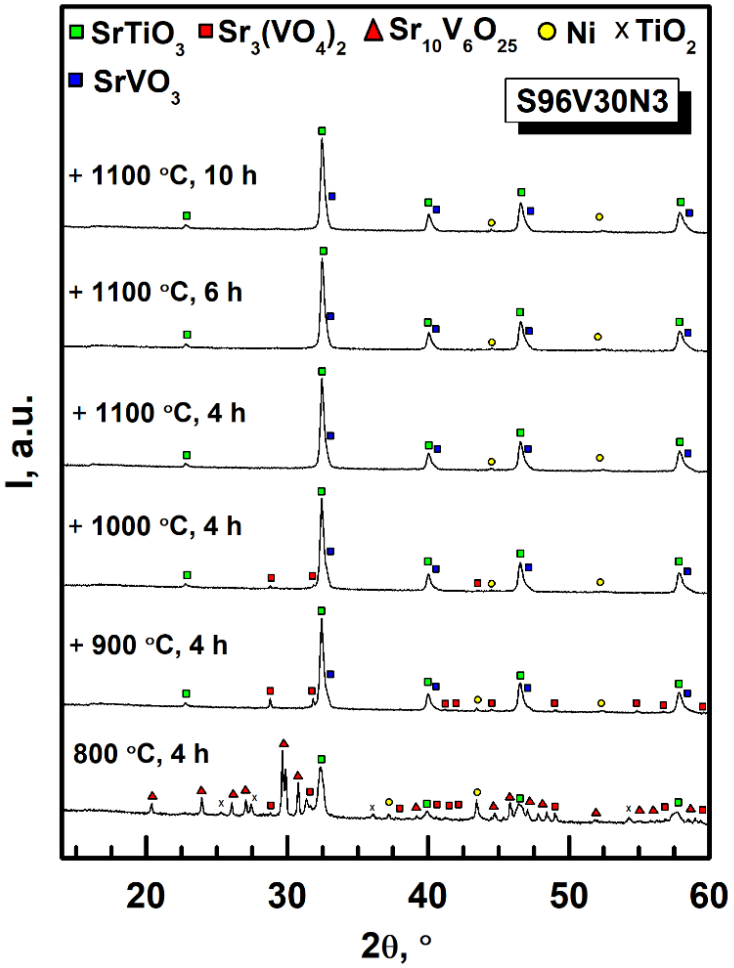


**Figure 3.10: XRD patterns of S96V30N3 after consecutive thermal treatment steps (from bottom up) at 800-1100 °C.**

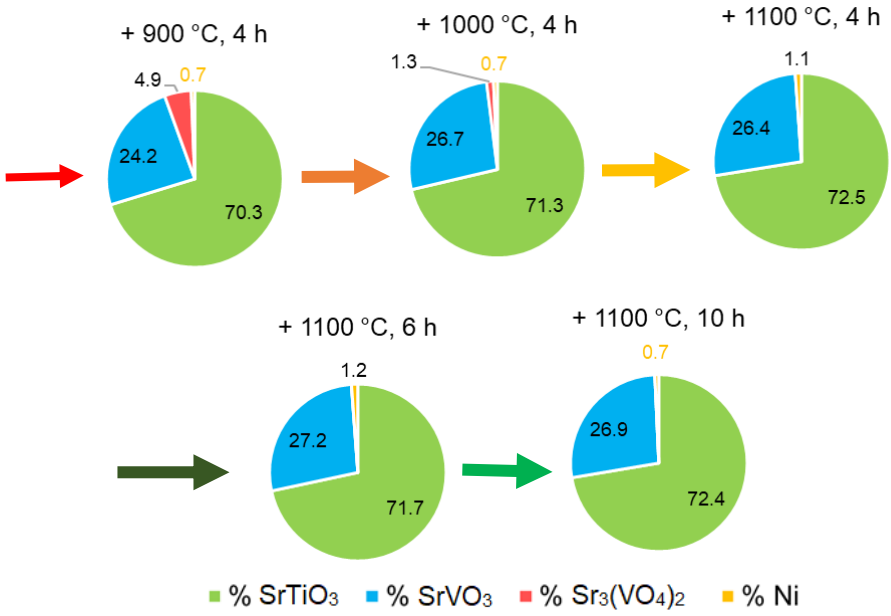


**Figure 3.11: Estimated fractions of different phases in S96V30N3 sample after consecutive firing steps at 900-1100 °C.**

Although 1100 °C would not be the final step for single-phase perovskite for some compositions, increasing the firing time would reveal helpful on potentially achieving elimination of $Sr_3(VO_4)_2$ phase.

### 3.1.4. Final thermal treatment procedure

The analysis of results discussed in subsections 3.1.2 and 3.1.3 can be summarized in the form of the following conclusions:

a) Ni does not tend to substitute into B-sublattice of $Sr(Ti,V)O_3$ perovskites in the course of thermal treatments under 10% $H_2$-$N_2$ atmosphere at temperatures ≥ 800°C and segregates as metallic phase;
b) Due to this, increasing Ni content in the nominal composition results in an excess of Sr and, consequently, promotes the formation of strontium orthovanadate $Sr_3(VO_4)_2$. The latter is a quite stable phase and is an intermediate during the solid-state synthesis of $SrVO_3$ perovskite under reducing conditions. [17] Typically, heat treatments at temperatures above 1000 °C are required to eliminate this phase. [17,25]
c) Calcinations at 1100 °C for up to 20 h are still insufficient to provide the formation of a single $Sr(Ti,V)O_3$ perovskite-type phase combined with metallic nickel.

Therefore, the final synthesis temperature was selected to be 1200 °C which should be low enough to avoid significant grain growth. Fresh mechanochemically-treated precursors of all compositions were pelletized and sintered at 1200 °C for 10 h. The results of subsequent XRD analysis (Figs. 3.12 and 3.13) demonstrated that the samples with a higher nominal Ni content combined with a lower or zero A-site deficiency (namely, SV30N6, SV40N12 and S98V30N9) still contained $Sr_3(VO_4)_2$ impurity. These compositions were therefore excluded from further work. The presence of the second perovskite phase was still suspected for at least one of other samples (as implied by asymmetry of the XRD reflections). Therefore, remaining six compositions were fired in the pelletized form for additional 20 h at 1200 °C to ensure the formation of single perovskite phase combined with a fraction of metallic Ni (Fig. 3.14). These samples were powdered and then used for the preparation of electrode layers and ceramic samples for electrical and dilatometric measurements.

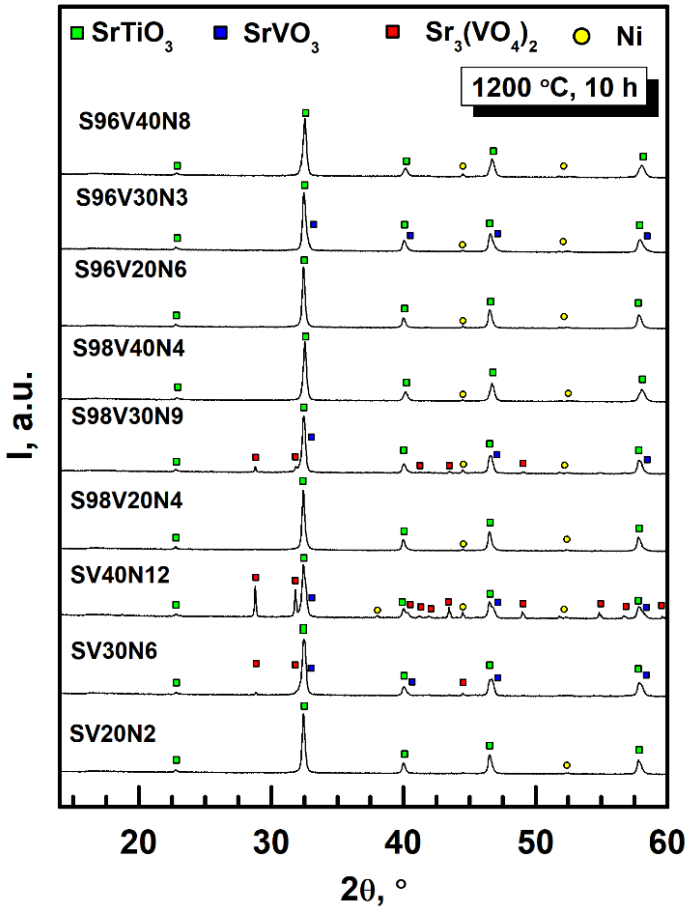


**Figure 3.12: XRD patterns of the samples sintered at 1200 °C for 10 h.**

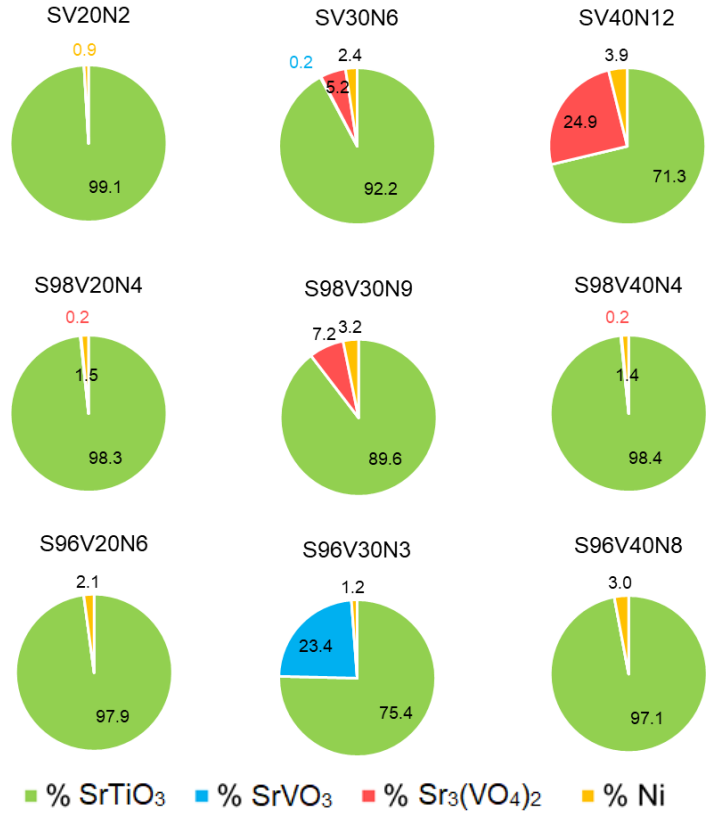


**Figure 3.13: Estimated fractions of different phases in samples sintered at 1200 °C for 10 h.**

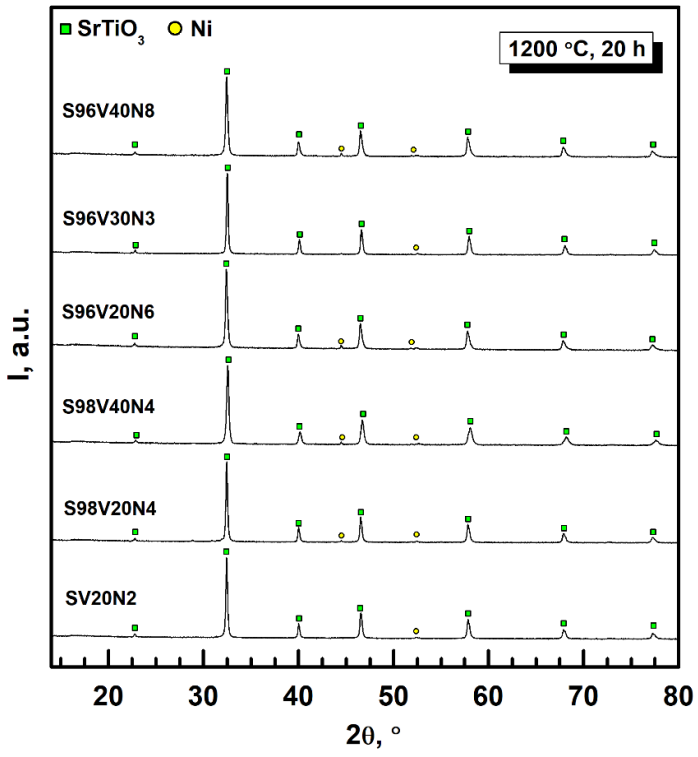


**Figure 3.14: XRD patterns of the samples sintered at 1200°C for additional 20 h.**

## 3.2. Crystal structure and microstructure of ceramic samples

XRD analysis showed that both the final powders (total heat treatment time 30 h at 1200 °C) and sintered ceramic samples (1450 °C, 10 h) comprised $Sr_{1-x}Ti_{1-y}V_yO_{3-\delta}$ solid solution with cubic perovskite lattice (space group *Pm-3m*), isostructural to the parent $SrTiO_3$ and $SrVO_3$ perovskites, and a fraction of metallic nickel (Fig. 3.14). The calculated lattice parameter (Table 3.1) showed a general tendency to decrease with increasing vanadium content in agreement with the data on $Sr(Ti,V)O_3$ system [31,47] ; the only exception from this trend is S96V40N8 sample.

**Table 3.1: Crystal lattice parameters and density of sintered STVN ceramics**

| Sample | *a (*Å) | Theoretical density (g/cm$^3$) | Experimental density (g/cm$^3$) | Relative density (%) |
|---|---|---|---|---|
| SV20N2 | 3.9000(1) | 5.16 | 4.93 | 95.5 |
| S98V20N4 | 3.9006(1) | 5.11 | 4.91 | 95.9 |
| S98V40N4 | 3.8868(2) | 5.19 | 4.89 | 94.4 |
| S96V20N6 | 3.9018(1) | 5.07 | 4.70 | 92.7 |
| S96V30N3 | 3.8956(1) | 5.09 | 4.53 | 88.9 |
| S96V40N8 | 3.9024(1) | 5.09 | 4.96 | 97.4 |

Note: theoretical density is roughly estimated from the crystallographic data assuming the nominal cation composition and stoichiometric oxygen content.

Sintered ceramic samples for most compositions were dense with relative density of 93-97% of theoretical and a small fraction of closed pores. The relative density of S96V30N3 ceramics was slightly lower (89%), but still not far from other compositions.

At the same time, the microstructure of the sample varied strongly with the composition (Fig. 3.15), apparently, due to different sinterability under identical sintering conditions. SEM images of fractured S96V30N3 ceramics showed a microstructure with well-distinguishable individual small grains with the sizes in the range 0.5–3.5 μm and with visible porosity, in agreement with the value of relative density (Table 3.1). The microstructure of S96V20N6 ceramics was closer to S96V30N3 samples, with small grains (1.5–6.0 μm), but with their shape implying the onset of sintering process with formation of denser agglomerates. Ceramic samples SV20N2 and S98V20N4 comprises small grains (2–10 μm), but also well-sintered dense inclusions with sizes up to 50 μm and

indistinguishable individual grains in these inclusions. Note that distribution of elements (Sr, Ti and V) was similar in both small grains and larger dense sections, within the accuracy of EDS analysis. Finally, fractured cross-sections of S98V40N4 and S96V40N8 represented dense sintered bodies with mostly indistinguishable individual grains. One may assume two possible factors responsible for different sinterability: (i) increasing vanadium content promotes the sintering with formation of dense ceramics with indistinguishable individual grains in fractured surface; (ii) strontium deficiency in the perovskite lattice has an opposite effect, and sintering results in formation of small easily distinguishable grains. The latter is effective mainly for S96V30N3 which, probably, is the only one composition which remains A-site deficient assuming that all Ni is segregated as a separate phase.

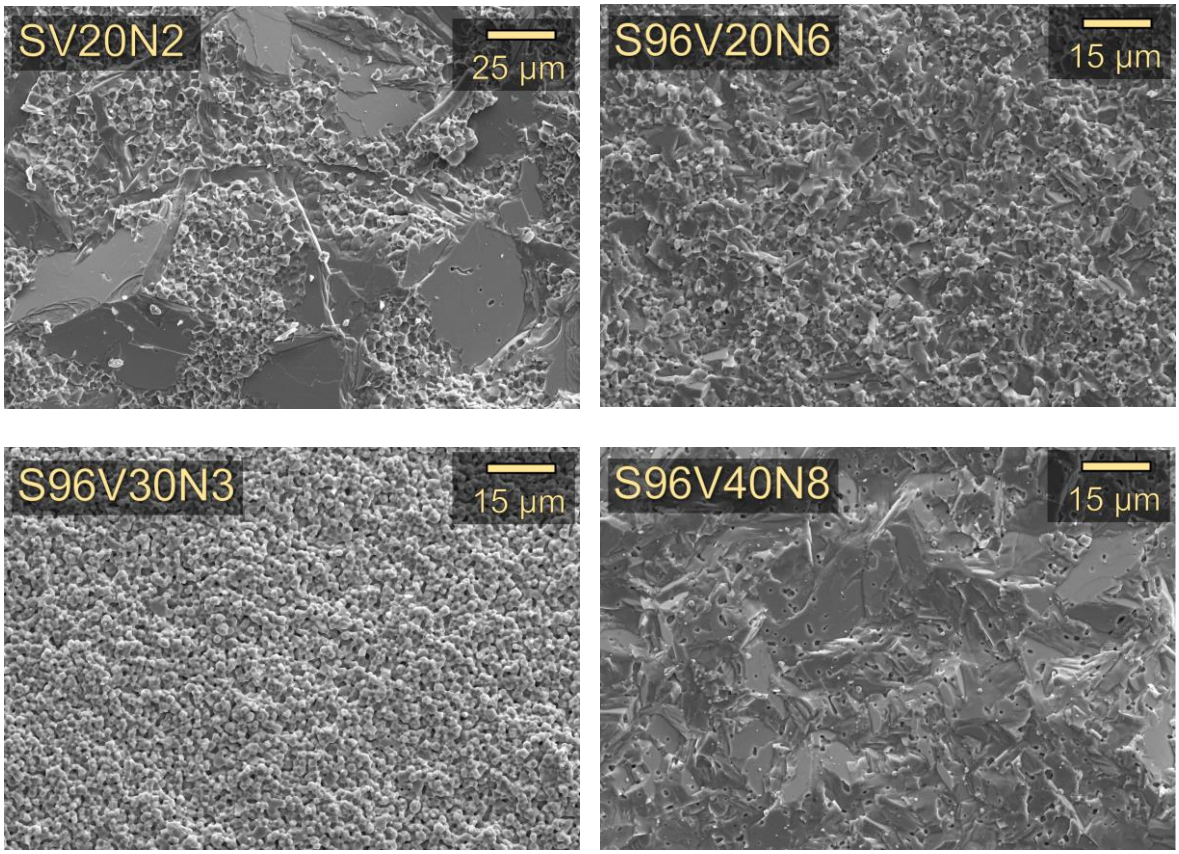


**Figure 3.15: SEM micrographs of fractured surface of STVN ceramics samples sintered at 1450°C.**

The segregation of metallic Ni was easily detected by SEM/EDS in ceramic samples for all compositions (Fig. 3.16). The size of spherical Ni particles varies to some extent with the composition. The samples with denser microstructure (S98V40N4 and S96V40N8) comprised larger Ni particles with sizes up to ~1 µm, while the areas with well-defined individual grains of the perovskite phase had inclusions of more evenly distributed smaller

Ni inclusions with sizes 0.2-0.7 μm (as in SV20N2 and S98V20N4 ceramics). Nevertheless, visible agglomeration of metallic nickel phase does not exclude completely the possibility of partial incorporation of Ni cations into B-sublattice of $Sr(Ti,V)O_{3-\delta}$ perovskites.

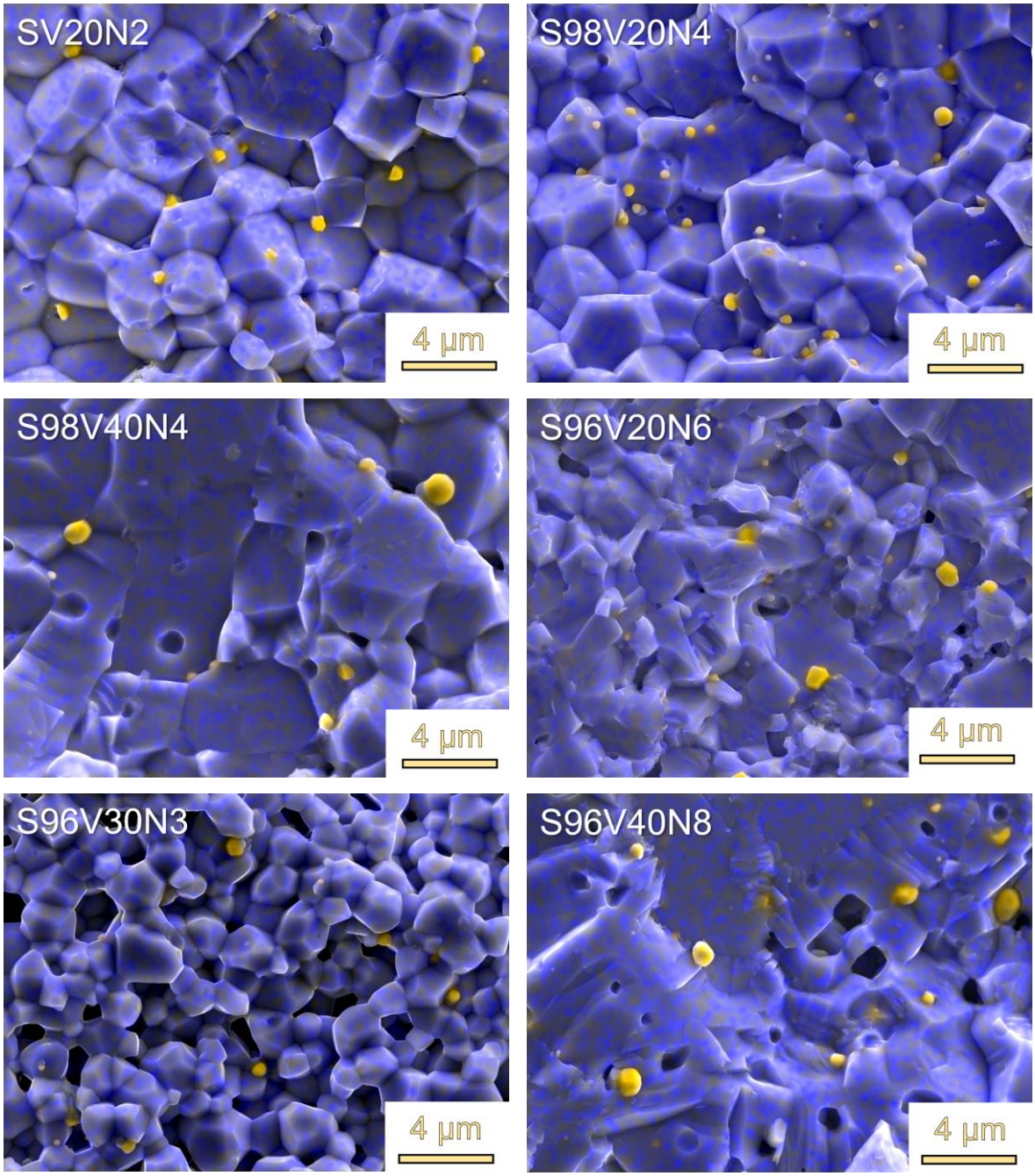


**Figure 3.16: SEM micrographs of fractured surface of STVN ceramic samples with overlaid EDS elemental mapping (blue: Ti; yellow: Ni).**

### 3.3. Thermomechanical compatibility with solid electrolyte

The dilatometric curves of all STVN ceramics showed a smooth slightly non-linear behavior on heating in reducing 10% $H_2$-$N_2$ atmosphere (Fig. 3.17). As for $SrTi_{1-x}V_xO_{3-\delta}$ ceramics [31] and other $SrVO_3$-based vanadates, [21,26,28] increasing deviation from the linear thermal expansion at higher temperatures can be partly attributed, most probably, to a minor contribution of chemical expansion associated with the variable oxygen content in the perovskite lattice.

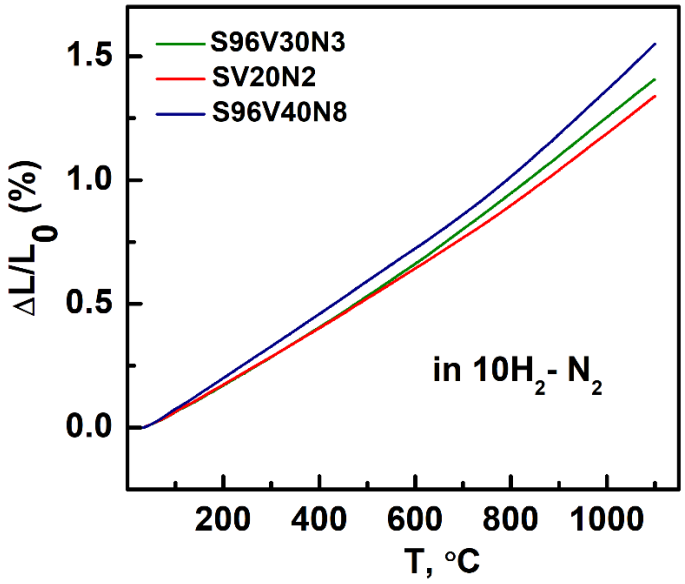


**Figure 3.17: Dilatometric curves of STVN ceramics on heating in 10%$H_2$-$N_2$ atmosphere**

The linear thermal expansions coefficients (TEC) estimated from the dilatometric data are listed in Table 3.2. All prepared ceramic materials exhibited rather similar average TECs varying in the range 12.5–14.3 ppm/K in the studied temperature range (25–1100 °C) and generally decreasing with increasing titanium content in the perovskite lattice. Similar observations were reported earlier for the $SrVO_3$-$SrTiO_3$ solid solutions; [31] increasing titanium content was found to suppress both true thermal expansion and chemical strain and to decrease the TEC values from 19.3 ppm/K for undoped $SrVO_{3-\delta}$ to 12.0 ppm/K for titanium-rich $SrTi_{0.9}V_{0.1}O_3$ at 100–1000 °C.

The values of TEC of STVN ceramics exceeds slightly that of common YSZ solid electrolyte (Table 3.2) but are still very close. This should ensure the thermomechanical compatibility between porous STVN electrodes and YSZ solid electrolyte ceramics in the course of temperature cycling.

**Table 3.2: Average thermal expansion coefficients of STVN ceramics in 10% $H_2$-$N_2$ atmosphere at 25-1100 °C.**

| Composition | Average linear TEC (ppm $K^{-1}$) |
|---|---|
| SV20N2 | 12.5 |
| S98V20N4 | 12.6 |
| S98V40N4 | 14.0 |
| S96V20N6 | 13.0 |
| S96V30N3 | 13.3 |
| S96V40N8 | 14.3 |
| YSZ [48] | 11.0 |

## 3.4. Electrical conductivity

All prepared STVN ceramics were found to exhibit semiconducting behavior under reducing conditions, with conductivity increasing on heating (Fig. 3.17). Electrical conductivity was found to increase with increasing vanadium content in the perovskite lattice of $Sr_{1-x}(Ti,V)O_{3-\delta}$. This is accompanied with a decrease of activation energy of electrical conductivity (Table 3.3). These observations are in good agreement with the data reported for the $SrVO_3$-$SrTiO_3$ pseudobinary system. [31] $SrVO_{3-\delta}$ is known to be a metallic conductor with conductivity level as high as ~ $10^3$ S/cm at 700-900°C. [17,25] On the other hand, undoped $SrTiO_3$ is a wide-bandgap semiconductor with conductivity below $10^{-1}$ S/cm at 900°C under similar reducing conditions. [49,50] Decreasing vanadium content in $SrTi_{1-y}V_yO_{3-\delta}$ solid solutions was observed to result in gradual decrease of electrical conductivity and a transition from metallic to semiconducting behavior. [31,47] This was interpreted in terms of gradual change in conductivity mechanism. For the compositions with vanadium contents below intermedium (~20-40 at. % in the B sublattice), one may expect the predominant electronic transport by electrons localized on titanium cations (equivalent to $Ti^{3+}$) possibly contributed by electron hopping between adjacent $V^{4+}/V^{3+}$ pairs. The probability of percolation between vanadium cations increases with increasing vanadium content, thus resulting in an increase in electrical conductivity.

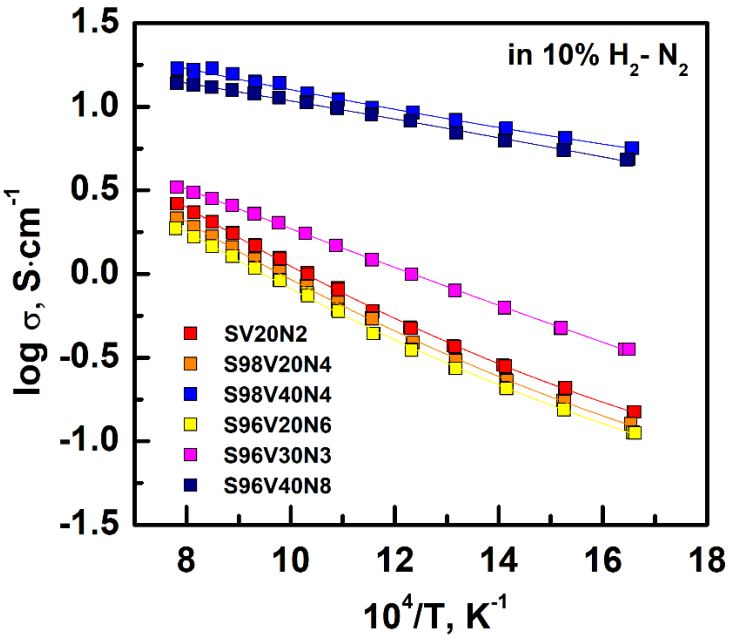


**Figure 3.18: Temperature dependence of electrical conductivity of STVN ceramics.**

**Table 3.3: Activation energy of electrical conductivity of STVN ceramics.**

| Composition | $E_A$ (kJ/mol) |
|---|---|
| SV20N2 | 35.2 |
| S98V20N4 | 35.1 |
| S98V40N4 | 18.2 |
| S96V20N6 | 34.8 |
| S96V30N3 | 29.2 |
| S96V40N8 | 17.7 |

Another observation is that, for the compositions with identical nominal vanadium content, the conductivity decreases with increasing nominal nickel content. While the true defect chemistry of the prepared perovskite phases remains questionable (whether there are still some remaining fractions of nickel cation in B-sublattice or not), one still may consider the following possible explanation assuming segregation of all (or almost all) nickel as a separate phase. In that case, simple estimations show that the perovskite phase for

only one composition, S96V30N3, will remain A-site deficient (assuming the full occupancy of B sites in the perovskite lattice). In all other cases, there will be an access of strontium which is to be accommodated either in a form of an impurity phase (in quantities too low to be detected by XRD or by a brief SEM/EDS inspection), or in a form of extended defects, such as rock-salt layers in Ruddlesden-Popper $Sr_{n+1}Ti_nO_{3n+1}$ phases. Either option would have a negative effect of the total conductivity of STVN ceramics.

Similar to titanium-rich $SrTi_{1-y}V_yO_{3-\delta}$ solutions, [31] prepared STVN ceramics exhibit a rather weak dependence of electrical conductivity on oxygen partial pressure $p(O_2)$ (Fig. 3.19). In general, the conductivity increases with reducing $p(O_2)$, which can be mainly attributed to the reduction of titanium cation and generation of electronic charge carriers as a results of oxygen release from the perovskite lattice:

$$2Ti^{4+} + O^{2-} \rightarrow 2Ti^{3+} + V_O + 0.5O_2 \qquad \text{(Equation 14)}$$

or

$$O^{2-} \rightarrow 2e^- + V_O + 0.5O_2 \qquad \text{(Equation 15)}$$

where $V_O$ is the oxygen vacancy. The slope of *log σ – log p(O₂)* dependence increases with decreasing vanadium content, thus reflecting an increasing contribution of titanium cations to the total electronic transport.

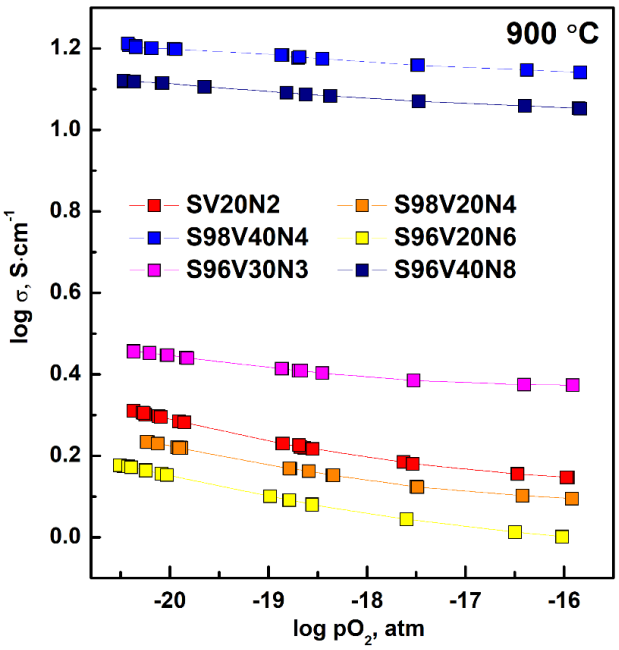


**Figure 3.19: Electrical conductivity of STVN ceramics on oxygen partial pressure at 900°C.**

Considering the electrode applications in solid electrolyte cells, high electrical conductivity is one of the main requirements to the electrode material. It should be as high as possible to minimize the ohmic losses of electrode and to avoid possible negative effects on electrochemical performance. It is generally considered that the minimum required electronic conductivity corresponds to > 1 $S.cm^{-1}$ for porous structures and one order of magnitude higher value for the bulk materials. [51] In the case of dense STVN ceramics, the conductivity of the compositions with the highest vanadium content, S98V40N4 and S96V40N8, corresponds to 10–17 $S.cm^{-1}$ at 700–900 ºC (Figs. 3.18 and 3.19) which seems to be acceptable for the application. Other materials exhibit 5–12 times lower conductivity in this temperature range. Thus, comparatively low electrical conductivity might be one the factors limiting the electrochemical performance of corresponding porous electrodes.

## 3.5. Electrochemical properties

For the electrochemical studies, porous electrode layers were applied onto both sides of dense YSZ pellets and sintered as described in subsection 2.7.1. SEM confirmed formation of porous layers with uniform microstructure and thickness of 35–45 μm (Fig. 3.20, A and C). The electrode layers consisted of submicron STVN particles with sizes in the range of ~0.1–0.6 μm, sometimes in agglomerates up to ~1.5 μm (Fig. 3.20, B and D). Inspection by SEM/EDS also detected the presence of agglomerated Ni particles, also with sizes of ~0.25–0.6 μm (Fig. 3.20, E and F). Possible existence of smaller Ni particles and their distribution on the surface of STVN porous structures could not be verified with the resolution of employed SEM/EDS equipment.

The polarization resistance ($R_p$) of porous STVN electrodes in contact with YSZ electrolyte was studied in a humidified 10% $H_2$–$N_2$ atmosphere ($H_2O$ content of ~3 vol. %) at 700–900 °C, employing electrochemical impedance spectroscopy (EIS). In the beginning of each experiment, the sample was heated to 900 °C in flowing $H_2$–$H_2O$–$N_2$ atmosphere and left overnight for equilibration. The measurements were performed in stepwise cooling regime with equilibration at each temperature for at least 1 hour.

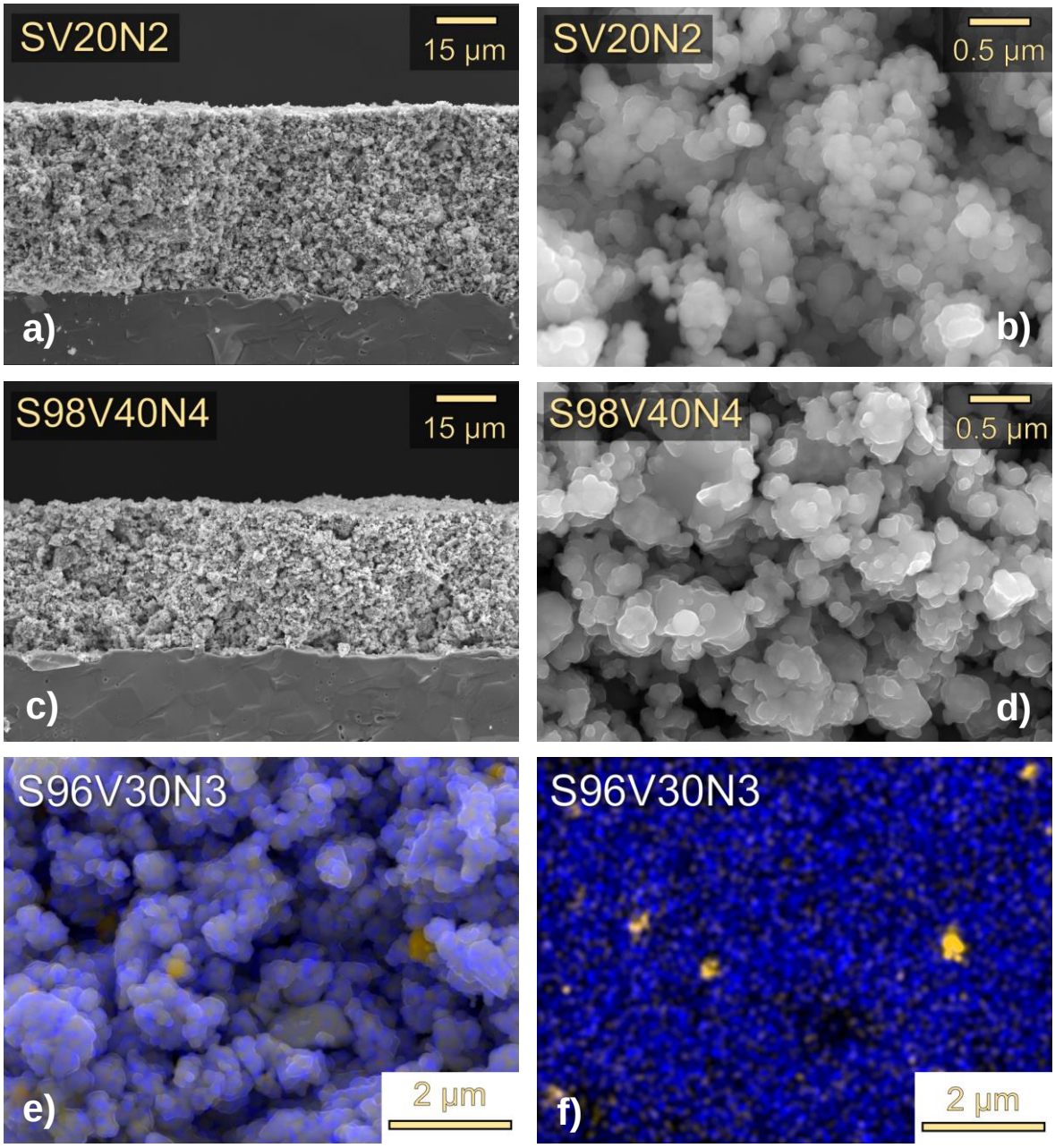


**Figure 3.20: SEM micrographs of SV20N2/YSZ (a, b) and S98V40N4/YSZ (c, d) half-cells: fractured cross-section (a,c) and magnified view of electrode microstructure (b,c). SEM/EDS images of fracture cross-section of S96V30N3 electrode: (e) SEM image with overlaid EDS elemental mapping, and (f) corresponding EDS elemental mapping (blue: Ti; yellow: Ni).**

One examples of a typical impedance spectrum of symmetrical STVN/YSZ/STVN cell is presented in Fig.3.21. The values of electrode polarization resistance were subtracted by fitting the experimental data to a simple equivalent circuit (inset in Fig.3.21) which included several element connected in series: inductance (L, a platinum wires contribution), ohmic resistance ($R_{ohm}$) of the cell, and two low-frequency (LF) R‖CPE contributions (where CPE

is a constant phase element) to the total polarization resistance. [52,53] Basically, the overall electrode contribution is represented on the plot (Fig. 3.21) by two distorted overlapping semicircles, and the difference between Z' values corresponding to the low-frequency and the high-frequency interceptions with Z' axis gives an approximate total $R_p$ value. Typical values of the specific pseudocapacitance for LF1 and LF2 contributions obtained by fitting the impedance spectra were of the order $10^{-6}$ and $10^{-4}$ $F.cm^{-2}$, respectively, as characteristic for the electrode processes. The first LF contribution (frequencies in the order of kilohertz) may be consistently associated with the microstructure of the electrode layers itself; this element is mostly temperature independent. Similar contributions have been satisfactorily fitted using R‖CPE sub-circuits with *n* values associated with the CPE element close to those that were obtained in the present work (i.e., =0.6). [54,55,56] The second LF contribution (*f* < 1 kHz) may be related to the gas diffusion and conversion processes (e.g. dissociative adsorption and/or species transfer). [57,58] This is a thermally-activated element.

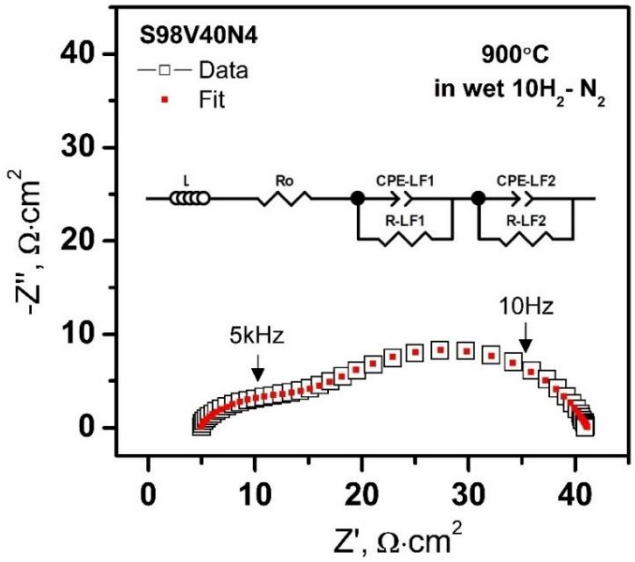


**Figure 3.21: Typical example of impedance spectrum of symmetric STVN/YSZ/STVN cell. Open and closed square symbols correspond to the experimental data and the results of fitting employing the equivalent circuit shown as the inset.**

The results of electrochemical characterization of STVN electrodes are presented in Figs. 3.22-3.24. Fig. 3.22 compares the impedance spectra of different electrodes at 900 °C, while Fig.3. 23 illustrated the evolution of impedance spectra for one of the electrode compositions with temperature. Temperature dependence of electrode polarization dependence for all materials is given in Fig. 3.24. The analysis of obtained data shows that all STVN electrodes exhibit rather poor electrochemical activity for hydrogen oxidation

reaction even at 900 °C. At this temperature, the specific $R_p$ values vary between 20 and 55 Ω×cm$^2$ (Figs. 3.22 and 3.24). Decreasing temperature reasonably results in a slower kinetics of electrode reaction, and polarization resistance exponentially increases on cooling (Figs. 3.23 and 3.24). The activation energy of the electrode process (reciprocal specific $R_p$) vary in a wide range from 95 to 140 kJ/mol (Table 3.4), although S96V30N3 and S96V20N6 electrodes exhibit the best and the worst performance, respectively, in the entire studied temperature range.

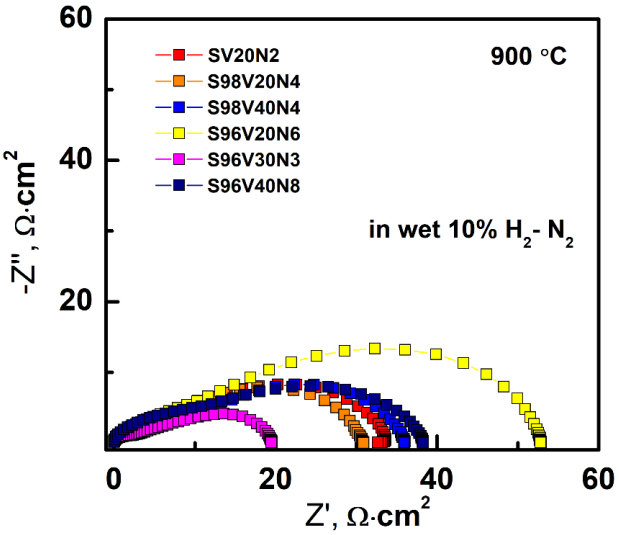


**Figure 3.22: Comparison of impedance spectra of STVN electrodes in contact with YSZ electrolyte at 900 °C. All spectra are corrected for ohmic resistance.**

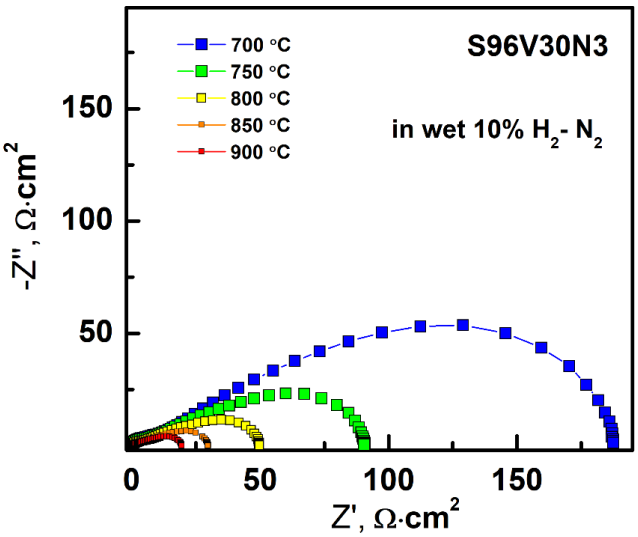


**Figure 3.23: Evolution of impedance spectra of S96V30N3 electrode with temperature. The spectra are corrected for ohmic resistance.**

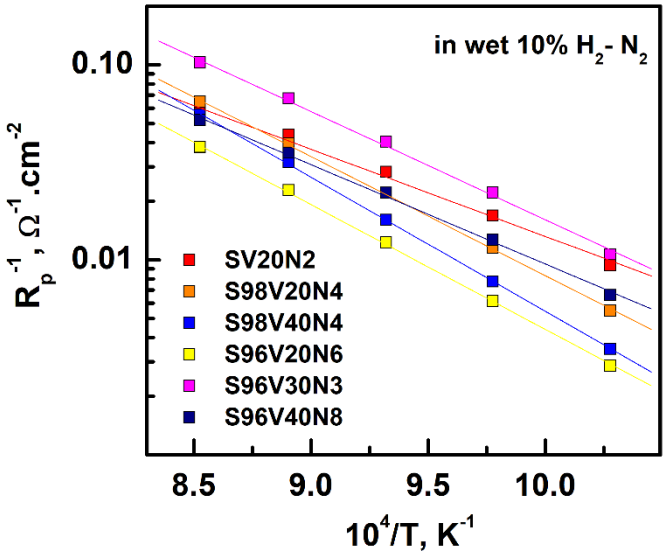


**Figure 3.24: Temperature dependence of reciprocal area-specific polarization resistance of STVN electrodes.**

**Table 3.4: Activation energy of electrode process ($1/R_p$) for porous STVN layers.**

| Compositions | $E_A$ (kJ/mol) |
|---|---|
| SV20N2 | 94.5 |
| S98V20N4 | 125.7 |
| S98V40N4 | 140.5 |
| S96V20N6 | 131.4 |
| S96V30N3 | 115.3 |
| S96V40N8 | 106.4 |

The analysis of the results did not reveal any evident correlations between the values of specific polarization resistance (Fig. 3.24), the activation energy of electrode process (Table 3.4), the electronic conductivity of electrode materials (Fig. 3.18) and the nominal nickel content (Table 2.2). One may conclude therefore that poor electrochemical performance of STVN electrodes should be attributed mainly to a poor intrinsic electrocatalytic activity of $Sr_{1-x}(Ti,V)O_{3-\delta}$ perovskites in combination with low expected ionic conductivity in these phases. High thermal treatment temperature required to eliminate unwanted $Sr_3(VO_4)_2$ impurity phase during the synthesis of $Sr_{1-x}(Ti,V)O_{3-\delta}$ promotes the agglomeration of nickel particles. As a result, the contents and specific surface area of nickel catalyst in the prepared STVN electrodes was insufficient to promote the electrochemical activity for the hydrogen oxidation reaction. Small differences in $R_p$ values of the prepared

electrodes (less than 3 times between the best and the worst electrodes at 900 °C) are causes, most likely, by slightly different uncontrolled distribution of segregated nickel particles in the electrodes.

### 3.6. Reactivity between electrode and electrolyte materials

Among other factors which typically have negative impacts on the electrode performance, one should mention a high-temperature reactivity between electrode and electrolyte materials in the course of fabrication and/or operation of electrochemical cell. This unwanted reactivity may result in a formation of insulating products at the interface between electrode and electrolyte which may block the mass transfer (diffusion of oxygen ions) across the interface and, thus, to deteriorate the electrochemical performance of the electrode.

In the present case, the inspections by SEM/EDS did not reveal the formation of any interdiffusion layers at the STVN/YSZ interface. As the thickness of such layers may be too low for the resolution of the technique, the next step was the calcination of as-prepared YSZ+STVN powder mixture (50:50 wt.%) at elevated temperature with subsequent XRD analysis of possible reactivity.

Fig. 3.25 shows an example of XRD patterns of YSZ+ S98V40N4 powdered sample before and after calcination at 1200 °C for 10 h under reducing conditions. Analysis of the XRD data revealed the appearance of a small additional peak at $2\Theta \approx 30.9°$ which may be assigned to $SrZrO_3$ perovskite-like phase. Formation of poorly conducting $SrZrO_3$ at the electrode/electrolyte interface is one the obstacles, for example, in utilization of classic $La_{1-x}Sr_xMnO_3$ cathodes in SOFC. [59] Nonetheless, the reactivity between YSZ and STVN under applied calcination conditions was found to be very limited. The electrode layers in the present work were sintered at lower temperature (1100 °C) and for shorter time (2 h). One may expect, therefore, a rather limited negative effect of possible reactivity between the materials on the electrode performance.

A common practice to improve the electrochemical activity of electrode materials with the predominant electronic conductivity and a poor ionic transport is to introduce a fraction of solid electrolyte material into electrode, thus forming a composite electrode. This results in a drastic increase of triple-phase boundary length (i.e. concentration of sites where the electrochemical reaction takes place) and, correspondingly, an improvement in electrochemical activity. As gadolinia-doped ceria (CGO) if often used for that purpose, the reactivity between CGO ($Ce_{0.9}Gd_{0.1}O_{2-\delta}$ in the present case) and STVN was tested in the similar manner as in the case of YSZ.

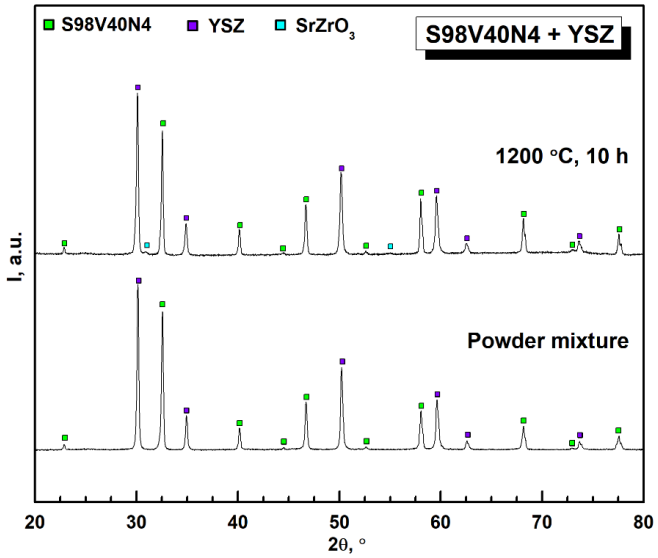


**Figure 3.25: XRD patterns of YSZ+S98V40N4 powder mixture before (bottom) and after (top) calcination at 1200 °C for 10 h in 10% $H_2$-$N_2$ atmosphere.**

The XRD patterns of CGO+STVN powder mixture (50:50 wt.%) before and after calcination at 1200 °C for 10 h are presented in Fig. 3.26. The careful inspection of the XRD data revealed the presence of several very small peaks on the background level of the XDRD pattern of the mixture after the calcination. Surprisingly, these tiny peaks coincide with positions of the reflections of $Sr_3(VO_4)_2$ phase. Independently of the mechanism of high-temperature reactivity between CGO and STVN, this reactivity is, again, very limited and is not expected to have a detrimental effect at temperatures below 1000 °C.

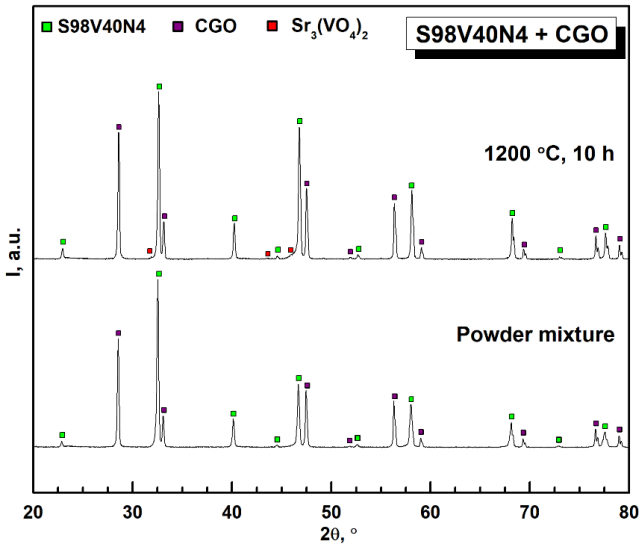


**Figure 3.26: XRD patterns of CGO+ S98V40N4 powder mixture before (bottom) and after (top) calcination at 1200 °C for 10 h in 10% $H_2$-$N_2$ atmosphere.**

## 3.7. Modification of electrochemical activity via infiltrations

The modification of STVN electrodes via incorporation of additional components, CGO as a solid electrolyte and nano-sized Ni as electrocatalyst, was attempted in order to improve the electrochemical performance. Two STVN materials, one with the best performance in unmodified form (S96V30N3) and one with the average performance (S98V40N4), have been selected for these studies. Three types of infiltrations were tried: only with CGO and with CGO+Ni with different Ni fractions (Ce:Gd:Ni ratios of 9:1:1 and 9:1:5). The procedure is described in subsection 2.7.2. The total fraction of infiltrated components corresponded to 21-30 wt. %, which gives the fraction of extra Ni catalyst equal to ~1 and ~4 wt. % and in the case of Ce:Gd:Ni ratios of 9:1:1 and 9:1:5, respectively. An illustration of the microstructure of modified electrode is shown in Fig. 3.27; SEM images revealed that porous STVN backbone is uniformly covered by submicron CGO particles with the average size 100-150 nm.

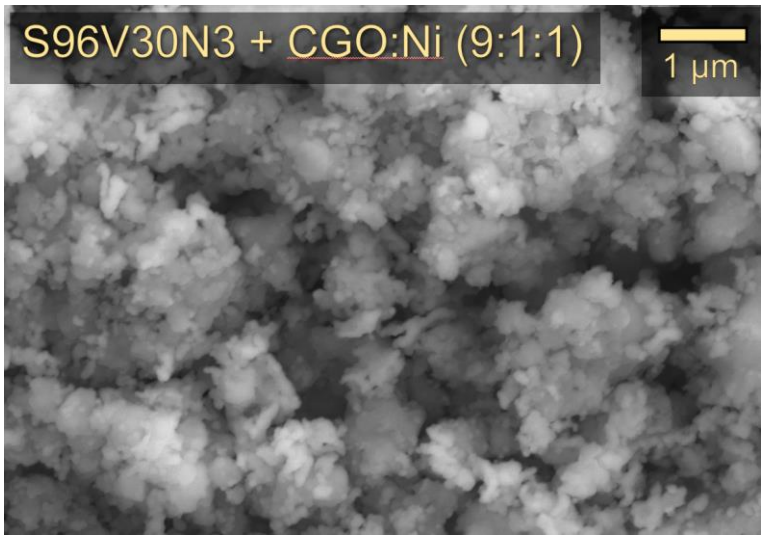


**Figure 3.27: SEM image showing the microstructure of S96V30N3 electrode infiltrated with CGO:Ni (Ce:Gd:Ni = 9:1:1).**

Figs. 3.28 and 3.29 compare impedance spectra of S98V40N4-& S96V30N3-based electrodes, respectively. Temperature dependence of specific polarization resistance of unmodified and infiltrated electrodes is presented in Fig. 3.30. As expected, the incorporation of CGO as a solid electrolyte component into STVN electrode reduced the polarization resistance. The effect was stronger in the case of S98V40N4 electrode which in the unmodified form showed worse performance; the $R_p$ value dropped by 4 times at 900 °C.

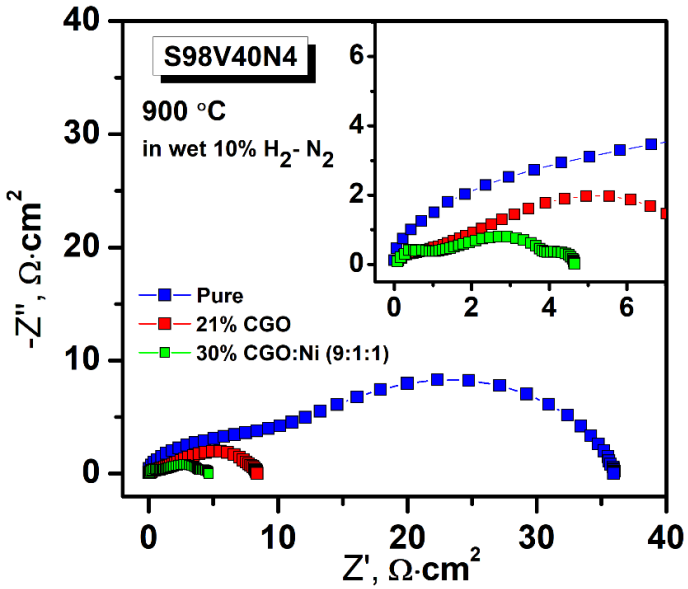


**Figure 3.28: Impedance spectra of bare and modified S98V40N4 electrodes at 900 °C. All spectra are corrected for ohmic resistance. Inset shows a magnified section of the plot.**

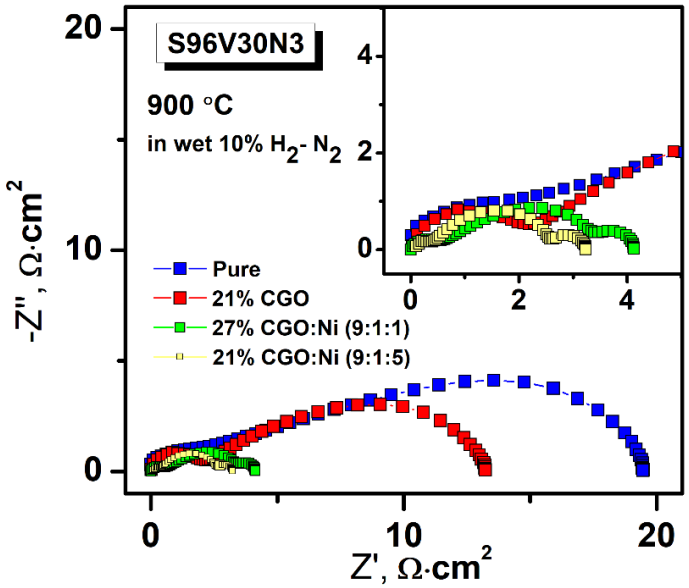


**Figure 3.29: Impedance spectra of bare and modified S96V30N3 electrodes at 900°C. All spectra are corrected for ohmic resistance.**

Infiltration of extra nickel resulted in a further improvement in the electrochemical activity of STVN-based electrodes (Figs. 3.28-3.30). This nickel is expected to be evenly distributed in a form of nanoscale particles over the surface of STVN and CGO components thus increasing drastically the concentration of catalytically active sites. The $R_p$ values for

STVN electrode layers co-infiltrated with CGO and Ni (Ce:Gd:Ni ratio of 9:1:1) decreases 5-7 times compared to the pristine electrodes at 900 °C. The incorporation of CGO or CGO in combination with extra nickel also gradually decreased the activation energy of the electrode process (Table 3.5). As a result, the relative improvements in electrochemical performance were even larger at lower temperatures (Fig. 3.30). Interestingly, the values of activation energy for infiltrated S98V40N4 and S96V30N3 electrodes becomes similar. In addition, the $R_p$ values for these two electrode compositions are very close to each other after infiltration by CGO+Ni (Fig.3.30). This seems to imply that STVN backbone play a rather passive role in terms of electrocatalytic activity in the case of infiltrated electrodes. Further increase in the fraction of infiltrated Ni by 5 times was observed to have comparatively small effect on the polarization resistance of S96V30N3-based electrodes (Figs. 3.29 and 3.30).

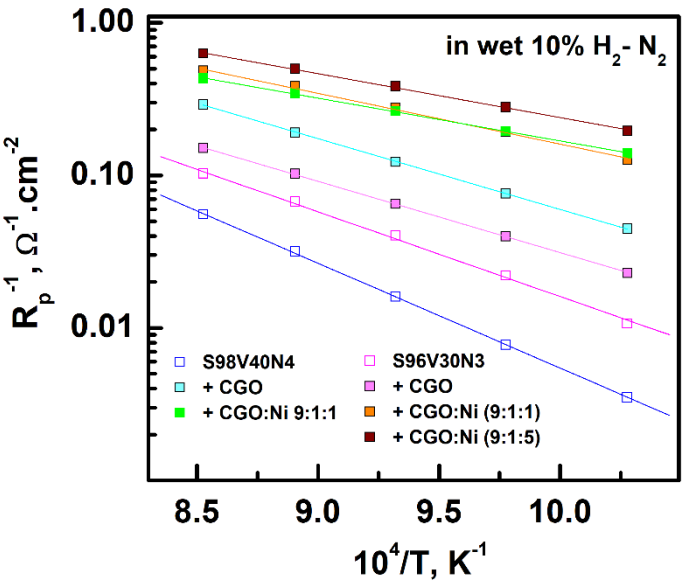


**Figure 3.30: Temperature dependence of reciprocal area-specific polarization resistance of S98V40N4- and S96V30N3-based electrodes.**

Polarization resistance of S98V40N4 infiltrated sample with CGO:Ni 9:1:1 was in fact smaller than when added more Ni to the solution. S96V30N3 samples had a more stable trend, where CGO:Ni 9:1:5 presented the smaller $R_p$ values. Infiltration with CGO seems to put both compositions to a similar activation energy. For CGO:Ni samples, activation energy dropped even more, although higher quantity of Ni did not have the same effect on both samples.

**Table 3.5: Activation energy of electrode process ($1/R_p$) for porous S98V40N4- and S96V30N3-based electrodes.**

| Composition | Infiltration | $E_A$ (kJ/mol) |
|---|---|---|
| S98V40N4 | - | 140.5 |
| | CGO | 97.8 |
| | CGO:Ni 9:1:1 | 62.6 |
| S96V30N3 | - | 115.3 |
| | CGO | 98.4 |
| | CGO:Ni 9:1:1 | 72.6 |
| | CGO:Ni 9:1:5 | 64.0 |

## 4. Conclusions

i) Room-temperature high-energy mechanochemical treatment of STVN precursor mixtures, for a reasonably short time interval to avoid a contamination, do not result in the crystallization of the desired phase, but promote a homogenization of precursors;

ii) Detailed analysis of the phase formation in selected STVN in the course of thermal treatments at 800-1200 °C under reducing conditions demonstrated that, due to the high stability of $Sr_3(VO_4)_2$ intermediate, the formation of desired products (comprising only $Sr_{1-x}(Ti,V)O_{3-\delta}$ cubic perovskite and metallic Ni) requires prolonged calcinations at 1200 °C;

iii) Due to this, nickel segregates as submicron metallic particles and is unlikely to substitute into the B-sublattice of the $Sr_{1-x}(Ti,V)O_{3-\delta}$ perovskite solid solutions (at least, in effective amounts) under applied thermal treatment conditions;

iv) Prepared STVN ceramics exhibit moderate average thermal expansion coefficients compatible with that of YSZ solid electrolyte;

v) Electrical conductivity of sintered STVN ceramics generally increases with an increase in vanadium content in the perovskite phase, while the nominal A-site deficiency has an opposite effect;

vi) Porous STVN electrodes applied onto YSZ solid electrolyte demonstrate rather poor electrochemical activity for hydrogen oxidation reaction. This can be attributes to several factors including low intrinsic electrocatalytic activity of $Sr_{1-x}(Ti,V)O_{3-\delta}$ perovskites, low expected ionic transport in these phases, and also segregation of Ni particles resulting in a low concentration of catalytically-active sites;

vii) Electrochemical performance of STVN electrodes can be improved by modifications via infiltration, namely, introduction of fractions of CGO as an ionically-conducting component and a small extra amount of well-dispersed Ni as an electrocatalyst;

viii) The implementation of the initial idea (low-temperature preparation of Ni-substituted titanate-vanadate with in-situ Ni exsolution under controlled redox conditions) requires, however, the assessment of other techniques for low-temperature synthesis (i.e. “soft chemistry” routes).

## 5. References


[1] C. Zuo, M. Liu, M. Liu, *Solid Oxide Fuel Cells*, in: M. Aparicio, A. Jitianu, L. Klein (eds.), *Sol-Gel Processing for Conventional and Alternative Energy*, Springer-Verlag New York (2012), 7–31

[2] R. Elder, D. Cumming, M.B. Mogensen, in: P.S. Elsje, A. Quadrelli, K. Armstrong, *Carbon Dioxide Utilisation: Closing the Carbon Cycle*, Elsevier (2014), 183–194

[3] S.Y. Gómez, D. Hotza, *Current developments in reversible solid oxide fuel cells*, Renewable and Sustainable Energy Reviews 61 (2016) 155–174

[4] X. Zhang, Y. Song, G. Wang, X. Bao, *Co-electrolysis of $CO_2$ and $H_2O$ in high-temperature solid oxide*, Journal of Energy Chemistry 26 (2017) 839–853

[5] S.C. Singhal, *Solid Oxide Fuel Cells*, The Electrochemical Society Interface (2007) 41–44

[6] N. Mahato, A. Banerjee, A. Gupta, S. Omarc, K. Balania, *Progress in material selection for solid oxide fuel cell technology: A review*, Progress in Materials Science 72 (2015) 141–337

[7] A.J. Jackobson, *Materials for Solid Oxide Fuel Cells*, Chemistry of Materials 22 (2010) 660–674

[8] Y. B. Lin, Z. L. Zhan, J. Liu, S. A. Barnett, *Direct operation of solid oxide fuel cells with methane fuel*, Solid State Ionics 176 (2005) 1827

[9] S.P.S. Shaikh, A. Muchtar, M.R. Somalu, *A review on the selection of anode materials for solid-oxide fuel cells*, Renewable and Sustainable Energy Reviews 51 (2015) 1–8

[10] F.S. Da Silva, T.M. De Souza, *Novel materials for solid oxide fuel cell technologies: A literature review*, International Journal of Hydrogen Energy 42 (2017) 26020-26036

[11] T. Chen, W.G.Wang, H. Miao, T. Li, C. Xu, *Evaluation of carbon deposition behavior on the nickel/yttrium-stabilized zirconia anode-supported fuel cell fueled with simulated syngas*, Journal of Power Sources 196 (2011) 2461

[12] Y.H. Heo, J.W. Lee, S.B. Lee, T.H. Lim, S.J. Park, R.H. Song, C.O. Park, D.R. Shin, *Redox-induced performance degradation of anode-supported tubular solid oxide fuel cells*, International Journal of Hydrogen Energy 36 (2011) 797

[13] B.C.H. Steele, P.H. Middleton, R. A. Rudkin, *Material science aspects of SOFC technology with special reference to anode development*, Solid State Ionics 40–41 (1990) 388-393

[14] X. Liu, K. Sohlberg, *Theoretical calculations on layered perovskites: implications for photocatalysis*, Complex Metals 1 (2014) 138

[15] W.H. Kan, A.J. Samson, V. Thangadurai, *Trends in electrode development for next generation solid oxide fuel cells*, Journal of Materials Chemistry A 4 (2016) 17913-17932

[16] Xiao-Ming Ge, Siew-Hwa Chan, *Solid Oxide Fuel Cell Anode Materials for Direct Hydrocarbon Utilization*, Advanced Energy Materials 2 (2012) 1156–1181

[17] J. Macías, A.A. Yaremchenko, J.R. Frade, *Redox transitions in strontium vanadates: Electrical conductivity and dimensional changes*, Journal of Alloys and Compounds 601 (2014) 186–194

[18] M. Gong, X. Liu, J. Trembly, C. Johnson, *Sulfur-tolerant anode materials for solid oxide fuel cell application*, Journal of Power Sources 168 (2007) 289-298

[19] X.M. Ge, S.H. Chan, Q.L. Liu, Q. Sun, *Solid oxide fuel cell anode materials for direct hydrocarbon utilization*, Advanced Energy Materials 2 (2012) 1156-1181

[20] J.S. Park, J. Luo, L. Adijanto, J.M. Vohs, R.J. Gorte, *The stability of lanthanum strontium vanadate for solid oxide fuel cells*, Journal of Power Sources 222 (2013) 123-128

[21] A.A. Yaremchenko, B. Brinkmann, R. Janssen, J.R. Frade, *Electrical conductivity, thermal expansion and stability of Y- and Al-substituted $SrVO_3$ as prospective SOFC anode material*, Solid State Ionics 247–248 (2013) 86–93

[22] M.J. Rey, Ph. Dehaudt, J.C. Joubert, B. Lambert-Andron, M. Cyrot, F. Cyrot Lackmann, *Preparation and structure of the compounds $SrVO_3$ and $Sr_2VO_4$*, Journal of Solid State Chemistry 86 (1990) 101–108

[23] V. Giannakopoulou, P. Odier, J.M. Bassat, J.P. Loup, *$SrVO_3$ and $Sr_2VO_4$, electrical properties below and above room T*, Solid State Communications 93 (1995) 579–583

[24] G.V. Bazuev, G.D. Milova, O.V. Makarova, *Synthesis and properties of solid solutions with perovskite structure in the $SrVO_3$-$EuVO_3$ system*, Inorganic Materials 17 (1981) 247–250

[25] S. Hui, A. Petric, *Conductivity and stability of $SrVO_3$ and mixed perovskites at low oxygen partial pressures*, Solid State Ionics 143 (2001) 275–283

[26] J. Macías, A.A. Yaremchenko, J.R. Frade, *Enhanced stability of perovskite-like $SrVO_3$-based anode materials by donor-type substitutions*, Journal of Materials Chemistry A 4 (2016) 10186–10194

[27] K.Z. Fung, S.Y. Tsai, C.Y. Liu, *Synthesis and Properties of Perovskite Anode for SOFC Applications*, ECS Transactions 57 (2013) 1423-1428

[28] J. Macías, A.A. Yaremchenko, D. P. Fagg, J.R. Frade, *Structural and defect chemistry guidelines for Sr(V,Nb)$O_3$-based SOFC anode materials*, Physical Chemistry Chemical Physics 17 (2015) 10749-10758

[29] C.D. Savaniu, J.T.S. Irvine, *Reduction studies and evaluation of surface modified A-site deficient La-doped $SrTiO_3$ as anode material for IT-SOFCs*, Journal of Materials Chemistry 19 (2009) 8119–8128

[30] A.A. Yaremchenko, S.G. Patrício, J.R. Frade, *Thermochemical behavior and transport properties of Pr-substituted*, Journal of Power Sources 245 (2014) 557-569

[31] J. Macías, A.A. Yaremchenko, E. Rodríguez-Castellón, M. Starykevich, J.R. Frade, *Compromising Between Phase Stability and Electrical Performance: $SrVO_3$–$SrTiO_3$ Solid Solutions as Solid Oxide Fuel Cell Anode Components*, ChemSusChem 12 (2019) 240-251

[32] J. Macías, *$SrVO_3$-based anode materials for hydrocarbon-fueled solid oxide fuel cells*, PhD Thesis, University of Aveiro (2017)

[33] A. Davarpanah, A.A. Yaremchenko, D.P. Fagg, J.R. Frade, *Ni-YSZ cermets for solid oxide fuel cell anodes via two-step firing*, International Journal of Hydrogen Energy 39 (2014), 15046-15056.

[34] T. Z. Sholklapper, H. Kurokawa, C.P. Jacobson, S.J. Visco, L.C. De Jonghe, *Nanostructured Solid Oxide Fuel Cell Electrodes*, Nano Letters 7 (2007), 2136-2141

[35] D. Ding, L. Xiaxi, S. Yuxiu Lai, K. Gerdesb, M. Liu, *Enhancing SOFC cathode performance by surface modification through infiltration*, Energy Environ. Sci. (2014) 7, 552

[36] Z. Liu, B. Liu, D. Ding, M. Liu, F. Chen, C. Xia, *Fabrication and modification of solid oxide fuel cell anodes via wet impregnation/infiltration technique*, Journal of Power Sources 237 (2013) 243-259

[37] Z. Liu, B. Liu, B. Liu, D. Ding, M. Liu, F. Chen, C. Xia, *Fabrication and modification of solid oxide fuel cell anodes via wet impregnation/infiltration technique*, Journal of Power Sources 237 (2013) 243-259

[38] S.P. Jiang, *Nanoscale and nano-structured electrodes of solid oxide fuel cells by infiltration: Advances and challenges*, International Journal of Hydrogen Energy 37 (2012), 449-470

[39] G. Yang, W. Zhou, M. Liu, Z. Shao, *Enhancing electrode performance by exsolved nanoparticles: a superior cobalt-free perovskite electrocatalyst for solid oxide fuel cells*, ACS Applied Materials and Interfaces 8, 51 (2016) 35308-35314

[40] J. Ishihara, *Nanomaterials for Advanced Electrode of Low Temperature Solid Oxide Fuel Cells (SOFCs)*, Journal of the Korean Ceramic Society 53 (2016) 469-477

[41] L. Thommy, O. Joubert, J. Hamon, M.T. Caldes, *Impregnation versus exsolution: Using metal catalysts to improve electrocatalytic properties of LSCM-based anodes operating at 600 °C*, International Journal of Hydrogen Energy 41 (2016) 14207-14216

[42] X. Ding, H. Liu, Z. Gao, Z. Gao, G. Hua, L. Wang, L. Ding, G. Yuan, *$La_{0.6}Ca_{0.4}Fe_{0.8}Ni_{0.2}O_{3-\delta}$ - $Sm_{0.2}Ce_{0.8}O_{1.9}$ composites as symmetrical bi-electrodes for solid oxide fuel cells through infiltration and in-situ exsolution*, International Journal of Hydrogen Energy 42 (2017) 24968-24977

[43] Y. Sun, M. Wang, J.L. Luo, *In-situ Exsolution of Nano Transition Metal Particles on Lanthanum Chromite Perovskite Anode for Solid Oxide Fuel Cells*, ECS Transactions 68 (2015) 1541-1548

[44] Y. Sun, J. Li, Y. Zeng, *A-site deficient perovskite: the parent for in situ exsolution of highly active, regenerable nanoparticles as SOFC anodes*, Journal of Materials Chemistry A 3 (2015) 11048

[45] J. Rodriguez-Carvajal, *Recent advances in magnetic structure determination by neutron powder diffraction*, Physica B: Condensed Matter 1932 (1993) 55

[46] S.H. Jensen, P.H. Larsen, M. Mogensen, *Hydrogen and synthetic fuel production from renewable energy sources*, International Journal of Hydrogen Energy 32 (2007) 3253-3257

[47] H. Tsuiki, K. Kitazawa, K. Fueki, *The donor level of $V^{4+}$ and the metal-nonmetal transition in $SrTi_{1-x}V_xO_3$*, Japanese Journal of Applied Physics 22 (1983) 590-596

[48] Yttria Stabilized Zirconia, YSZ, Matweb – Material Property Data, retrieved from: http://www.matweb.com/search/datasheet.aspx?MatGUID=4e3988dd9adb4d1ca37a1b2cbab87d9a (accessed 31 October 2019)

[49] N.H. Chan, R.K. Sharma, D.M. Smyth, *Nonstoichiometry in $SrTiO_3$*, Journal of Electrochemical Society 128 (1981) 1762-1769

[50] J.C.C. Abrantes, A.A.L. Ferreira, J.A. Labrincha, J.R. Frade, *Electrical conductivity of $Sr_{1-x}TiO_{3-\delta}$ materials*, Ionics 3 (1997) 436-441

[51] A. Atkinson, S. Barnett, R.J. Gorte, J.T.S. Irvine, A.J. McEvoy, M. Mogensen, S.C. Singhal, J. Vohs, *Advanced anodes for high-temperature fuel cells*, Nature Materials 3 (2004) 17-27

[52] J. Jamnik, J. Maier, *Treatment of the impedance of mixed conductors equivalent circuit model and explicit approximate solutions*, Journal of Electrochemical Society 146 (1999) 4183-4188

[53] J.R. Macdonald, *Impedance Spectroscopy Emphasizing Solid Materials and Analysis*, Wiley, New York (1987)

[54] S. Primdahl, M. Mogensen, *Oxidation of hydrogen on Ni/yttria-stabilized zirconia cermet anodes*, Journal of Electrochemical Society 144 (1997) 3409-3419

[55] B. A. Boukamp, *A nonlinear least squares fit procedure for analysis of immittance data of electrochemical systems*, Solid State Ionics 20 (1986) 31-44

[56] M. Brown, S. Primdahl, M. Mogensen, *Structure/performance relations for Ni/yttria-stabilized zirconia anodes for solid oxide fuel cells*, Journal of Electrochemical Society 147 (2000) 475-485

[57] S. Primdahl, M. Mogensen, *Gas conversion impedance: A test geometry effect in characterization of solid oxide fuel cell anodes*, Journal of Electrochemical Society 145 (1998) 2431-2438

[58] S. Primdahl, M. Mogensen, *Gas diffusion impedance in characterization of solid oxide fuel cell anodes*, Journal of Electrochemical Society 146 (1999) 2827-2833

[59] S.P. Jiang, *Development of lanthanum strontium manganite perovskite cathode materials of solid oxide fuel cells: a review*, Journal of Materials Science 43 (2008) 6799-6833